Summer 2017

Interpreting the dynamics of submarine landslides through hydroacoustic modeling, West Mata volcano, NE Lau Basin

Jonathan G. Drobiarz
drobiaj@wwu.edu

Interpreting the dynamics of submarine landslides through hydroacoustic modeling, West Mata volcano, NE Lau Basin

By

Jonathan Drobiarz

Accepted in Partial Completion

of the Requirements for the Degree

Master of Science

Kathleen L. Kitto, Dean of the Graduate School

ADVISORY COMMITTEE

Chair, Dr. Jacquelin Caplan-Auerbach

Dr. Pete Stelling

Dr. Brady Foreman

Dr. Robert Dziak

Master's Thesis

In presenting this thesis in partial fulfillment of the requirements for a master's degree at Western Washington University, I grant to Western Washington University the non-exclusive royalty-free right to archive, reproduce, distribute, and display the thesis in any and all forms, including electronic format, via any digital library mechanisms maintained by WWU.

I represent and warrant this is my original work, and does not infringe or violate any rights of others. I warrant that I have obtained written permissions from the owner of any third party copyrighted material included in these files.

I acknowledge that I retain ownership rights to the copyright of this work, including but not limited to the right to use all or part of this work in future works, such as articles or books.

Library users are granted permission for individual, research and non-commercial reproduction of this work for educational purposes only. Any further digital posting of this document requires specific permission from the author.

Any copying or publication of this thesis for commercial purposes, or for financial gain, is not allowed without my written permission.

Jonathan Drobiarz
July 17, 2017

Interpreting the dynamics of submarine landslides through hydroacoustic modeling, West Mata volcano, NE Lau Basin

A Thesis
Presented to
The Faculty of
Western Washington University

In Partial Fulfillment
Of the Requirements for the Degree
Master of Science

by
Jonathan Drobiarz
June 2017

Abstract

Landslides are an integral process in the development of submarine volcanoes, but these events are rarely recorded and observed. Therefore, understanding how the morphology of volcanoes evolve requires information on landslides. Hydroacoustic signals were analyzed for the purposes of characterizing frequent landslides on West Mata volcano during a 5-month eruptive period. Over 200 landslide signals have been compared in conjunction with hydroacoustic modeling to better understand the dynamics that control them. We used interference patterns produced by multipath rays to identify and model these slope failures. Landslides were most clearly captured on the north and west stations, suggesting a source on the western face of West Mata. This is consistent with a zone of high sediment accumulation previously found by bathymetric depth difference mapping. Landslides were found to initiate ~200-300 m below the summit and travel at speeds of 4-8 m/s, and possibly up to 20 m/s. Slope failures were observed during periods of high eruptive activity suggesting failure by unstable tephra loading preferentially at sites of previous sliding. Landslides at West Mata also tend to occur in clusters with decreasing run out distances over time. It is recommended that future studies involve a denser hydrophone network to better locate landslides and model slide mechanics.

Acknowledgements

I would like to thank and acknowledge the following important people:

My thesis committee:

- **Dr. Jacqueline Caplan-Auerbach** (WWU) for her encouraging words of wisdom, patience, help with understanding the data/hydroacoustic model, revisions on my thesis and giving me the opportunity to work on this fantastic project.
- **Dr. Pete Stelling** (WWU) for his revisions and helpful comments on my thesis.
- **Dr. Brady Foreman** (WWU) for his revisions and helpful comments on my thesis.
- **Dr. Robert Dziak** (NOAA, Pacific Marine Environment Laboratory; Oregon State University) for his time in helping me complete my thesis.

Delwayne Bohnenstiehl, Andy Lau, Haru Matsumoto, and Matt Fowler, participants in the NSF-funded cruises to West Mata, which gathered the data used in my thesis.

Jim Long (WWU, IT Specialist with the College of Science and Engineering) for helping me configure the hydroacoustic modeling program for use on my personal computer.

Family, fellow graduate students, and friends for your support in making this a truly worthwhile and memorable time while completing my Master's degree.

This project was funded by the **Western Washington University Geology Department** and the **Western Washington University Graduate School.**

Table of Contents

List of Figures

List of Tables

I. Introduction

Submarine landslides are a ubiquitous process that actively shape both continental margins and submarine volcanoes. Perhaps the best known event occurred in 1929 as a result of the Grand Banks earthquake, which broke a network of cable lines off the coast of Newfoundland (Hampton et al., 1996). Submarine landslides range in magnitude from the large catastrophic slumps, to the less imposing shallow slope failures (Okal, 2003; Masson et al., 2006). Past events are typically studied through bathymetric imaging, but this provides us with no indication of how frequently they occur or how they are triggered. Studying an active submarine volcano where landslides are common could help to answer those questions.

Submarine landslides have been identified at West Mata volcano, Lau Basin, with a characteristic spectral pattern of interference from multipathing rays (Matsumoto et al., 2011; Caplan-Auerbach, Dziak, et al., 2014; Dziak et al., 2015). The goal of this study is to use the interference pattern on multiple hydrophones from slides over a 5-month span in conjunction with hydroacoustic modeling to interpret landslide source depth and velocity. Connections between slope failures and the volcanic eruption are made to help understand the critical role landslides have in the development of submarine volcanoes.

II. Background

2.1 Submarine landslides and causes

Submarine landslides commonly occur on volcanic flanks that are over steepened with fragmental material (Masson et al., 2006). Broadly, submarine slope failures are influenced by elevated fluid pressures produced by rapid sediment deposition or abrupt seismic shaking. Physical models using sand and flour showed that slope failures on volcanic cones may be triggered by basal failure, unbuttressing due to the horizontal movement of a lateral wall, summit growth from sediment accumulation, and magmatic intrusion (Acocella, 2005). Experiments by Acocella (2005) showed that the sediment accumulation process resulted in shallow, clustered mass wasting that occurred in generally the same location, while the other processes produced deeper and more variably oriented tracks. Shallow, clustered slope failures were initially influenced by previous landslide scars, but over time those scars became less important and slides eventually distributed broadly across the cone.

Monowai, a submarine volcano in the Kermadec arc (SW to the Tonga arc) experiences frequent slope failures ranging from shallow debris avalanches to sector collapses during periods of eruption activity, resulting from unstable tephra loading (Chadwick et al., 2008). In 2002, a collapse event was captured by near shore seismometers, which recorded an unusual swarm of T-phases coming from Monowai volcano. Repeated bathymetric surveying helped to visualize where on the volcano these events occurred. It was found that slope failures were influenced by the explosive eruption style of Monowai, which led to unstable loading of high amounts of fragmental material on its slopes (Chadwick et al., 2008).

NW Rota-1, a Mariana arc submarine volcano produced frequent shallow and narrow slope failures with thicknesses and volumes similar to those at Monowai volcano, suggesting that this is a common mode of failure on pyroclastic loaded volcanic slopes (Chadwick et al., 2012). Mass wasting events were recorded on hydrophones and found to occur during high intensity volcanic eruption modes, suggesting a link between volcanic output and slope failure, consistent with observations at Monowai.

In the Canary Islands, slope failures were found to result from dike intrusion and sediment accumulation from volcanic eruptions (Krastel et al., 2001). Sedimentological evidence suggests that submarine landslides on the Canary Islands occur retrogressively (headwall is incrementally eroded backward by successive failures) and involve a series of failures that take place over the span of hours to days (Masson et al., 2006), but this mode of failure has not been observed in real time. More extensive geophysical investigations are required to back up or amend this assertion.

2.2. Hydroacoustic approach to studying landslides

Mass wasting events in the submarine realm have been investigated mainly through repeat bathymetric surveying and hydroacoustic approaches (Caplan-Auerbach et al., 2001; Chadwick et al., 2008; Clague et al., 2011; Chadwick et al., 2012; Embley et al., 2014; Caplan-Auerbach et al., 2014). Bathymetric difference mapping tells us that a slide occurred sometime between two surveys, and allows the calculation of slide volume, but this technique cannot be used to determine slide duration or whether the event was a single pulse or a series of multiple failures in the same region. Hydroacoustics is a more practical technique for constraining the timing of slide events. Hydrophones capture T (tertiary)

waves, compressional seismic waves that propagate vast distances through water (Ewing et al., 1950; de Groot-Hedlin and Orcutt, 1999; Caplan-Auerbach et al., 2001; Okal, 2011). Seismic energy from earthquakes couple into the water column at solid-liquid interfaces and travel within the SOFAR (SOund Fixing And Ranging) channel in the marine environment (Johnson, R, H. et al., 1963). The SOFAR channel is a region within the world's oceans that allows for long range, low velocity sound transmission (Figure 1). Vertical changes in temperature and pressure dictate how sound waves travel, with temperature the greater factor in the upper layers and pressure the greater factor in the deeper layers (NOAA Ocean Explorer website). The SOFAR channel contains the ideal combination of low temperature and low pressure that allows for sound waves to travel slowest. Because sound waves tend to bend toward regions of low velocity, sound waves then become trapped within this region and travel thousands of kilometers with minimal attenuation producing the ringing nature of T-phase wavetrains. Because of this, many oceanic sounds are recorded by hydrophones, including ship traffic and whale vocalization. The depth of the SOFAR channel varies around the world depending on temperature and salinity, but it typically falls between 600 and 1800 m (Okal, 2001). Placing hydrophones within this channel provides optimal conditions for recording long range signals within the world's oceans.

Frequent submarine landslides occurring on the submarine flank of Kilauea volcano were detected by the Hawaiian Undersea Geo-Observatory (HUGO) and Pacific Marine Environmental Laboratory (PMEL) hydrophone arrays (Caplan-Auerbach et al., 2001). HUGO was stationed about 35 km from Kilauea and the PMEL array sat ~ 5000 km away (Caplan-Auerbach et al., 2001). It was found that lava entering the sea accumulated a layer of hyaloclastites that would eventually fail and slide down the submarine coastal slope (Caplan-

Auerbach et al., 2001). The spectral signal associated with these slide events began with a low frequency rumble followed by a broadband coda often lasting minutes. The low frequency rumble was interpreted as the movement of large blocks and the broadband section caused by the downslope movement of unconsolidated material (Caplan-Auerbach et al., 2001).

Study on the fatal 1998 tsunami in Papua New Guinea revealed that a seismically induced submarine slump likely produced the devastating wave (Okal, 2003). Hydroacoustic waves generated by the landslide were detected by near shore seismometers through the conversion of hydroacoustic energy to seismic energy, allowing for the landslide to be well recorded on land. Based on source timing, tsunami dynamics, and signal character the most likely cause for the tsunami was a large underwater slump. A shipboard bathymetric survey later revealed evidence for a large, recent slump exactly in the proposed failure area. Understanding submarine landslide dynamics is a critical aspect of quantifying and anticipating coastal hazards.

NW-Rota-1 is the only other submarine volcano where a submarine landslide was recorded by an in situ hydrophone (Chadwick et al., 2012). Landslides were marked by high amplitude, broadband hydroacoustic signals lasting up to a couple of hours (Figure 2). Low frequency activity during these landslide signals suggests a link between the volcanic eruption and subsequent slope failures (Chadwick et al., 2012).

2.3. West Mata geologic setting and eruption history

West Mata volcano offers a good opportunity to study submarine landslides over the course of a prolonged eruption sequence (Caplan-Auerbach et al., 2014). West Mata sits in the NE Lau Basin, between the Tonga trench and the NE Lau Spreading Center (Figure 3). The tectonic regime is dictated by the westward subduction of the Pacific Plate under the Indo-Australian Plate (Baumberger et al., 2014). The presence of boninite lava suggests that West Mata lava is the result of direct partial melt of the upper mantle as a consequence of subduction (Kuroda et al., 1978; Resing et al., 2011). The Mata volcanoes appear slightly elongate resulting from en-echelon tear faulting within the basin and conical from clastic debris fans (Resing et al., 2011; Clague et al., 2011). Fine clastic debris produced by frequent pyroclastic eruptions coats the smooth flanks of the volcano with slopes up to 34-35° on the upper reaches (Clague et al., 2011). The smooth flanks relative to the rocky rift zones suggest the presence of thick sediment deposits. Chutes of volcanic sand are present on the upper slopes suggesting previous slope failures have occurred there (Clague et al., 2011). A May 2009 ROV dive revealed that slopes were covered with pyroclastic debris, sand, and broken and intact lava pillows (Merle, 2009).

From 2008 to 2012, West Mata experienced a complex, multiphase period of continuous eruptive activity that produced much of the observed hydroacoustic signal (Clague et al., 2011; Embley et al., 2014; Baumberger et al., 2014; Dziak et al., 2015). Eruption from two vents produced most of the volcanic output: Hades at 1200 m depth and Prometheus at 1174 m depth (Resing et al., 2011), (Figure 4). Observations from ROV dives have shown that Hades is associated with low lava fountains and Strombolian-style bubble bursts, and Prometheus with more explosive hydrothermal degassing, and fragmentation

(Dziak et al., 2015). Fragmentation from Prometheus results in a widespread distribution of clastic material on the upper slopes (Clague et al., 2011). Although, active secondary eruptive vents have been found and evidence exists of previous explosive pyroclastic activity deep down the volcanic flank (Clague et al., 2011). ROV investigations revealed lava flow, pillow formation, and vigorous effusive eruptions as all part of the eruptive process (Merle, 2009). Major avalanches of blocks and pyroclastic material were also seen bombarding the slopes just below the eruptive cone near the Hades vent, although acoustic data is not available for this time frame. Periods of harmonic acoustic tremor (20 – 100 Hz) are suggested to be associated with episodic fragmentation gas release events (Dziak et al., 2015). Signals <30 Hz are dominated by continuous eruption and volcanic tremor along with magma bubble bursts (Resing et al., 2011; Mack, 2014; Dziak et al., 2015). Repetitive, explosive degassing eruptions (Figure 5) dominate the hydroacoustic record suggesting an abnormally gas-rich activity at this depth (Resing et al., 2011). Diffuse periods of explosion tremor (lower panel Figure 5) were caused by violent degassing at Prometheus, which stops abruptly due to the formation of a magma quench cap (Mack, 2014; Dziak et al., 2015).

2.4 West Mata submarine landslides

The 2009-2010 West Mata hydroacoustic network included four stations recording for 5 months (Figure 3; Table 1). Each hydrophone was anchored to the ocean bottom with its receiver suspended within the SOFAR channel and recorded continuously at a sample rate of 1000 Hz. Volcanic and tectonic activity were recorded as well as ship traffic and whale vocalization, but those events were rare and easily distinguishable from geologic activity.

Caplan-Auerbach et al. (2014) were the first to use landslide spectral content as a means of locating the events and estimating average velocities. Submarine landslides at West Mata were identified as harmonic signals between 1 and 400 Hz lasting up to two minutes. The hydroacoustic signals from these landslides are comparable to those at Kilauea, which display a similar broadband, 100-200 s duration signal (Caplan-Auerbach et al., 2001). It was determined that slides traveled down the northern flank at average speeds between ~10-25 m/s based on depth difference mapping and hydroacoustic modeling using data from the north hydrophone (Caplan-Auerbach et al., 2014). This project extends and revises the work of Caplan-Auerbach et al. (2014) by comparing signals between multiple hydrophones to better interpret slide velocities and dynamics. Understanding why these landslides occur and how they relate to the eruption sequence provides further motivation for research.

III. Methods

3.1. *Spectrogram analysis*

The West Mata hydroacoustic data were visualized through 1-hour duration spectrograms, which allow the signal to be represented in terms of time, amplitude, and frequency up to 500 Hz (Figure 6). Frequencies above 400 Hz, however, were excluded due to the attenuation effects of the anti-aliasing filter. Hydroacoustic spectrograms clearly display dominant frequencies, allowing clear interpretation the type of process that generated the signal.

All four stations record alternating spectral bands of loud and quiet signal resulting from interference from multipath acoustic rays, a product of the Lloyd's Mirror effect (Figure 6). Direct and sea-surface reflected waves combine at the receiver to either enhance or diminish the captured signal (Matsumoto et al., 2011; Caplan-Auerbach, Dziak, et al., 2014).

Waves reflected off the sea surface experience a 180° phase inversion (Wilson, 2007) (Figure 7). Surface reflected waves travel further overall than direct waves between the source and receiver. Because the reflected wave is inverted, if the total distance traveled between those two ray paths differs by whole number wavelengths, the arrival of the two waves results in destructive interference, and the receiver will experience net transmission loss. The result is a spectrogram with alternating high and low amplitude signals. Equation 1a relates ray path difference to wavelength, a critical component to this interference effect:

Equation 1a. $\mathbf{dx = n\lambda}$

where dx is the added distance a surface reflected wave travels relative to a direct wave, λ is wavelength, and n is any integer value. Alternatively, interference can be determined by the time delay between direct and surface reflected waves: $dt = dx/v = n/v$, where v is velocity. Since $\lambda = v/f$, where f is frequency, this effect is dependent on the frequency of the propagating waves. Equation 1b relates frequency to differential travel time between rays:

Equation 1b. $$\boldsymbol{f = \frac{n}{dt}}$$

A long travel time delay between a surface reflected ray and a direct ray will result in interference at small increments of frequency, where detection depends on the sample rate. In contrast, slight differences in travel time would produce large frequency intervals of interference. Because interference bands are dependent on source receiver geometry, they are expected to remain constant with time at integer multiples of a certain frequency if the

distance between the source and receiver remain constant as well. Short term changes in interference frequency must indicate changes in the distance between the source and receiver. Matsumoto et al. (2011) observed constant interference bands recorded by a stationary hydrophone, but bands were not constant when recorded by an acoustic glider. As the glider moved toward West Mata, the frequency spacing between interference bands decreased due to increasing travel time delay between direct and surface reflected waves. If the receiver array is fixed, as is the case in this paper, changing interference frequencies must mean a moving source.

At West Mata, signals coming from the summit contain a constant pattern of interference frequencies, or spectral banding. But periodically, short term signals with a pattern of changing frequencies with time are recorded (Figure 8). All observed periods of changing interference bands exhibit a decrease in frequency. Because this spectral banding pattern is a result of an increase in travel time delay between direct and surface reflected waves, and because the hydrophone is anchored in place, the hydroacoustic source must be traveling towards the receiver, in this case downslope. Short term changes in interference are consistent with the occurrence of submarine landslides on West Mata (Caplan-Auerbach et al., 2014). Interference that increases in frequency would theoretically indicate a source moving away from the receiver. It is important to note that broadband peaks and nulls are intrinsic to the Lloyd's mirror phenomenon, not the Doppler effect. Narrow band tonal shifts is a consequence of the Doppler effect as a source moves past the receiver, which is not observed here (Wilson, 2007). Although spectral banding has been observed on submarine volcanoes other than West Mata, its pattern has not been used to study submarine landslides elsewhere (Johnson and Norris, 1972).

3.2. *Cataloging landslide signals*

Beginning in December 2009, each 1-hour segment of hydroacoustic data was studied to identify and catalog possible landslide signals. For selection, the signal must contain interference bands throughout the majority of the signal, and be clear enough to calculate the frequency spacing between bands. Additionally, the signal should be clear of noise which can decrease the clarity of the signal. Catalog details included event dates and signal arrival times, clarity of the interference bands, signal duration, interference spacing at the start of the signal, and interference spacing at the end of the signal (Appendix 3a). This process was performed for both the north and west hydroacoustic datasets. Although many landslides were documented for both hydrophones, only those captured clearly by both hydrophones were considered further. Rarely, slides were captured by the north station and absent on the west suggesting that those events were occurring in a different location than those detected by both instruments. Throughout the 5-month hydroacoustic record, landslide signals were ubiquitous on all hydrophones, but interference patterns were absent on the south and east hydrophones (Figure 9). Without spectral bands, landslides captured on the south and east hydrophones were not included in the cataloging process.

3.3. Confirming West Mata as a source for landslides

Because signals traveling in the SOFAR channel arrive from multiple localities and great distances, it is important to confirm that these landslides were in fact coming from West Mata (Ewing et al., 1950; Caplan-Auerbach et al., 2001). Ideally, arrival times are identified from the time series data, but landslide signal onsets are typically weak and difficult to identify with precision. Instead, approximate signal onsets were found by calculating the

envelope for a landslide on each hydrophone (Pulli and Upton, 2002). Signal arrivals were more easily compared by relative timing within the hydrophone array to confirm that they were coming from West Mata. Calculating the envelope first required applying a high pass filter (cutoff frequency = 100 Hz) to remove unrelated low frequency signals such as earthquake T-phases. Landslide signals are broadband so low frequencies can be cut out without significantly affecting the overall signal. Thus, the landslide becomes the dominant signature in the data. Next a low pass filter (cutoff frequency = 0.01 Hz) was applied to the absolute value of the previously filtered data to capture the wave envelope (Figure 10). This procedure was repeated for the same event on all four hydrophones. The arrivals for each station were plotted together to confirm that this particular landslide is consistent with a source on West Mata (Figure 11). Arrival times were calculated based on timing within data files and compared between the hydrophones. For selected events (Table 2), the southern hydrophone received the signal first, then the eastern, followed by the western, and last by the northern hydrophone. These delays are consistent with a source at West Mata with some degree of uncertainty due to lack of information about the local sound speed profile.

3.4. *Inferring the general landslide location*

West Mata volcano spans approximately 20 km^2 so narrowing down the general landslide source location is the primary goal of this study. The variable character of landslide signals on different hydrophones can be used to evaluate possible slide areas (Figure 9). Bathymetry can impact how well a signal is received by a given hydrophone; the volcano itself can block a signal, causing diminished wave amplitude resulting in weak signal capture. This would occur when a landslide is located on an opposite face of the volcano

relative to the hydrophone (Figure 12). Lack of interference pattern from particular hydrophones can help narrow down possible source locations. Only the north and west hydrophones record clear spectral banding during landslides. The south and east hydrophones lack the interference pattern during most of the events and the south hydrophone recorded the weakest signal of all four stations (Figure 9). Source-receiver geometry is not optimal for spectral banding on the south and east hydrophones when the source is on the opposite side of the volcano. If landslides were occurring on the SE flank, the southern hydrophone would clearly capture the signal first and display spectral bands in the hydroacoustic data (Figure 13). Interference bands were not observed during landslides from the southern station, which suggests that slope failures were not occurring on the SE flank, consistent with Caplan-Auerbach, et al., (2014).

3.5. *Bellhop modeling for source depth calculations*

Hydroacoustic modeling of interference patterns was used for the purposes of identifying landslide depths. Bellhop is a hydroacoustic model that allows for users to trace beams and model far-field marine transmission loss (Porter, 2011). Bathymetric profile, source depth, source frequency, sound speed profile, seafloor material parameters are all variables within the model. No sound speed profile local to West Mata exists, so a standard model was used (NOAA NODC). An average marine sediment density of 1.66 g/cc was implemented in all models (Tenzer and Gladkikh, 2014). Bathymetric profiles were extracted from GMRT (Global Multi Resolution Topography synthesis) through GeoMapApp using a 100 m resolution bathymetric grid ("GeoMapApp"; Ryan et al., 2009). Data point spacing along profiles was extrapolated from the bathymetric grid assuming a simplified slope face.

Coherent pressure beams were used for transmission loss modeling assuming a vacuum above the marine surface and an acoustic half space for the seafloor. Virtually 100% of sound energy reflects off the water-air interface so it is safe to assume a vacuum above the sea surface (Wilson, 2007). Sea surface roughness also affects the capture of surface reflected beams, which ultimately affects signal interference at the receiver. Because interference bands appear clear and discrete on the hydrophones, it is safe to assume that sea surface roughness is not a factor in signal capture at West Mata.

Over 200 landslides from the north and west hydrophones were modeled based on their changing interference frequencies (Figure 14). Using spectral band spacing at the beginning and end of the landslide signal, Bellhop was used to calculate source depths that would generate this pattern. After calculation, Bellhop produces an image spatially depicting how sound at a given frequency would propagate in the local submarine environment. Due to the effects of multipath ray interference, zones of loud signal (low transmission loss, bright colors) and quiet signal (high transmission loss, dark blue) are banded through the water column (Figure 15). If the receiver is located in a zone of high transmission loss, it would have recorded a quiet signal at that frequency and integer multiples of that frequency. For better clarity, sources were modeled using the second overtone, rather than the fundamental frequency. Doubling the signal frequency achieves the same transmission loss pattern, but with tighter depth resolution. An easier approach was to create an interference catalog by testing which frequencies would be quiet at depths along the slope of the volcano (Appendix 3b). Then spectral band spacing for each landslide was compared with known quiet frequencies to infer source depth. Modeling this way characterizes the relationship between interference spacing and depth: interference spacing decreases with depth (Caplan-Auerbach,

Dziak, et al., 2014). This approach is best used for small landslides, which can be modeled as point sources traveling downslope. Large landslides would behave as multiple point sources emitting from different depths and wouldn't produce the observed interference pattern by the addition of many ray path geometries.

3.6. Comparing north and west models

The technique described above can yield a variety of possible source depths. However, comparing the results between the two hydrophone models can eliminate some of these source locations. For example, a signal with interference spacing of ~30 Hz on the north station could be caused by a source at either ~1590m or ~1840m depth. The same signal on the west station has ~31 Hz spectral banding yielding a source depth of ~1570 m, but could not generate a source deep enough to produce a second possibility. Therefore, a source at 1840 m depth can be eliminated, increasing confidence in a source around ~1570 m and ~1590 m. Source depths between models were not averaged, rather kept separate to reduce averaging error. This same methodology was used for all documented landslides to help narrow down source depths.

3.7. Calculating landslide velocities

Velocity was calculated for each landslide using the time duration of the hydroacoustic signal and the total predicted distance that landslide traveled down the western slope based on modeling. Because modeling landslides resulted in a range of failure depths and termination depths for each event, minimum and maximum velocities were calculated.

The duration of the landslide signal was derived from the north station data because it captured a slightly clearer signal than the west station.

IV. Results

4.1. *Depth difference bathymetric maps*

Documented morphologic changes on West Mata helped narrow down a region for slope failures. Depth difference mapping between 2009 and 2010, the time period for landslides in this study, revealed a clear area of positive depth change on the western face interpreted as sediment accumulation from the eruption (Clague et al., 2011; Embley et al., 2014). Tephra and lava deposits accumulated just north of the WSW Rift Zone (WSWRZ), between 1400 m and 1700 m depth, an area referred to as the eruption period III (PIII) eruptives region (Embley et al., 2014). Figure 16 displays the small region of sediment accumulation used for hydroacoustic modeling. Additionally, high resolution bathymetry detailed steep slopes (~35°) at this depth range, approximately the angle of repose (Clague et al., 2011).

4.2. *PIII site models*

Bellhop models were oriented from the PIII eruptives region based on the fact that continuous material accumulation provides conditions optimal for slope failure. This region also contains pre-existing topographic channels through which sediment can more easily travel (Embley et al., 2014). Figure 17 displays the bathymetric transects used for hydroacoustic modeling. Landslide signals arriving at the east hydrophone do not display interference patterns, but are comparable in signal strength to the north and west

hydrophones. Slope failures in the PIII region could explain the lack of interference during slides on the east hydrophone because acoustic rays traveling northeast are shielded by the volcano. Prior to constraining depths, a proposed slide area was marked on the western flank, which contains the PIII region (Figure 18). This differs from the area proposed by Caplan-Auerbach et al. (2014) who hypothesized that landslides were occurring at the PI eruptive deposit on the northern flank (Figure 16). Landslides on the northern flank would display clear spectral banding on the eastern hydrophone, which is rarely observed. However, a few signals on the eastern hydrophone do exhibit spectral banding, suggesting that those events were occurring elsewhere on the volcano, possibly on the northern face. The proposed slide area containing PIII would also generate the weakest overall signal and lack of spectral bands on the southern hydrophone which is consistent with model results (Figure 19) and observed data.

4.3. *Constraining landslide source depths*

Landslides were modeled for a range of source depths. To constrain the proposed slide area, the maximum range of depths was calculated based on both north and west hydroacoustic models. Both models predict that the shallowest failure depth during this period occurred at ~1450 m. The furthest termination depth was to ~2280 m based on the north model and ~2070 m based on the west model (Figure 20). On average, landslides were contained within ~1550 m and ~1800 m (location errors are +/- 20 m, see section 4.6) consistent with the location of the PIII region. Landslide failure depths and termination depths were modeled for 214 events throughout the 5-month eruptive period, organized by date (Figure 21). A “threshold” separated failure depths from termination depths for each

model. At least 90% of landslides initiated above 1660 m based on the north hydrophone models and 1620 m based on the west hydrophone models. No evidence of slope change exists at these threshold depths. North models show the most common failure depths occur between 1530 m and 1571 m and west models show that the most common failure depths are between 1550 m and 1582 m (Figure 22). Landslide were compared overall between the north and west models for initiation depths and termination depths. Models were in better agreement for initiation depths than termination depths (Figure 23). The north models predicted slightly deeper termination depths than the west models. Each data point may represent a number of landslides that initiated at the same depth resulting in a plot appearing to have fewer samples.

4.4. *Landslide velocities*

Bellhop models predict velocities ranging from 1 – 11 m/s with a majority of slides traveling between 4-6 m/s (Figure 24). Because slides initiating at the summit cannot be ruled out, landslides may have traveled up to 15-20 m/s. A number of landslide velocities were in agreement between north and west models, with some events deviating by up to 7 m/s (Figure 25).

Average submarine landslide velocities have previously been modeled by Ward and Day (2002) using the following equation:

Equation 2. $$V = \sqrt{gLcsin\beta o/8}$$

where g is the acceleration due to gravity (9.8 m/s^2), L_c is the length of the slide from the block toe to the slide toe and β_o is the average slope angle in degrees. Using this equation, a slide length of ~400 m on a 35° slope, comparable to one on West Mata, should have an average velocity of ~20 m/s. From modeling, slide velocities were within the same order of magnitude, but at least 10 m/s slower than the equation estimates.

It was also noteworthy to examine whether a size relationship to slide velocity existed in the dataset. Ward and Day calculated slide velocities for large, tsunami generating submarine landslides, which could explain the higher velocities. Because slide area and volume for West Mata events were unknown, maximum slide length was plotted against velocity (Figure 26). Larger landslides (landslides that traveled further in this case) tend to move faster based on models from both the northern and western stations.

4.5. Slide cluster models

Throughout the 5-month monitoring period, landslides tended to occur in clusters, sometimes up to 35 events in a day (Figure 27). Slides have also been observed occurring just minutes apart (Figure 28). In an effort to understand the dynamics that control slide clusters, days with >10 landslides were examined closer. During these days, slides tended to initiate at a similar depth (~1550 m, +/- 20 m), but decrease in run out distance throughout the day (Figure 29).

4.6. *Uncertainties*

The 100 m bathymetric grid used for modeling provided some error when extracting profiles. Data point spacing was less than grid resolution so data points were inferred using

GeoMapApp (Ryan et al., 2009) assuming a simplified slope face. In addition, interference bands were most clearly visible in the middle of the event. They were often ambiguous at the beginning and end of the signal as sound levels dropped below background noise. Calculations of interference spacing were based on an average of visible quiet frequency bands. For example, if only three bands of quiet signal were clearly visible, frequency spacing was averaged over those three bands (Figure 30). Bellhop models can only be used for landslide signals that contained interference bands. Depths were modeled based on the first indication of interference, not the onset of the landslide signal. There is possibly a lag between when the landslide actually starts and when its signal rises above background noise to produce interference bands. Thus, the actual depth of landslide initiation in this study may be higher up the volcano flank. The same is true for the slide terminus: as the slide loses energy, its signal blends in with background noise, causing the interference bands to disappear. The overall broadband signal continues up to a minute after the disappearance of interference bands, which means material is probably still moving. Therefore, the actual terminus of the landslides could be further down the volcano flank, though its full extent isn't clear.

Changes in interference frequency controlled how precisely source depths could be modeled, as an acoustic source could produce the same hydroacoustic interference pattern within a given depth range. An acoustic source between 1571 m and 1608 m depth would display the same interference pattern on the north hydrophone (Figure 31). Therefore, Bellhop models are precise at this frequency to a depth range of about 40 m. On average, source depths for each modeled frequency have an error of approximately +/- 20 m. This error is probably due to the resolvability of wavelength when considering interfering acoustic

waves. Considering a 36 Hz acoustic wave in this marine environment (v = ~1482 m/s), its wavelength is approximately 41 m. Bellhop model resolution depends on the wavelength of the acoustic wave, meaning it cannot resolve source depth better than ~41 m in this case. However, no local sound speed profile exists so it is impossible to know exactly how well source depths can be resolved.

Maximum slide velocity was calculated using the maximum possible slant distance that landslide traveled, and a similar approach was taken to calculate the minimum slide velocity. At times, the maximum velocity of a slide differed from minimum velocity by up to 2 m/s, which reflects the sensitivity of source depth within models. However, velocity is more sensitive to the uncertainty of signal duration than source depth. Landslide signals ultimately blend in with background noise when they lose enough energy. Interference bands disappear quicker than the overall landslide signal causing error in event duration. Because landslide signals are present both before and after the appearance of interference bands by as long as 60 seconds, significant motion could have occurred that cannot be modeled. However, when comparing slide velocities this is a negligible effect because the distance and duration for each slide was determined by the presence of interference bands. For consistency, the duration of each landslide was determined by the presence of interference bands on the north station.

V. Discussion

5.1. Landslide source location

Repeat depth difference mapping by Embley et al. (2014) suggest that the most likely landslide source is on the western flank rather than the northern flank as was proposed by Caplan-Auerbach et al. (2014). However, the northern flank can't be entirely ruled out as some landslide signals lacked the interference pattern required for modeling. Signals lacking clear interference bands could be caused by sources from other locations on the volcano or from landslides large enough to reduce the effects of multi-path rays. Interference frequencies were also different between slides, meaning they initiated at various depths. Slight differences in source depths between models may have been caused by the lack of local sound speed profile, by assuming that sound wave propagation is uniform across the hydrophone network.

Broadly, landslides were found to occur between 1450 m and 2280 m depth, assuming they occurred on the western face, based on the interference patterns at the beginning and end of 214 landslide signals. Although slides initiating at depths below 1450 m are consistent with the PIII region, summit initiated slides cannot be ruled out. At times, landslide signals begin with a ~36 Hz interference pattern similar to that of eruption activity at the summit, but the same interference pattern could result from a source ~200 m down the flank in the PIII region. During the eruption, sediment is accumulating at the summit, which means mass wasting from there is possible. However, during the time frame of this study, significantly more material is accumulating in the PIII region than the summit (~ +25 m depth difference). For that reason, it is more likely that slides are occurring in PIII than at the summit. However, it is hard to justify mass wasting from the PIII region when the area

experienced an addition of 25 m of material. This suggests that there was an even greater initial deposition of material in the upper flank region of PIII. It is clear that modeling landslide source depths on West Mata proved more challenging than presumed.

5.2. *Landslides caused by volcanic activity*

Landslides at West Mata are only observed to occur during periods of high background hydroacoustic activity, consistent with observations on NW Rota-1 (Chadwick et al., 2012). At times, the landslide itself marks a change in background hydroacoustic character (Figures 10, 32). This suggests a correlation between landslides and increased hydroacoustic noise, but it's unclear as to what the noise represents. This increase in background noise could be caused by an increase in the overall eruptive energy release, changing from low frequency tremor to diffuse explosive degassing. Explosive eruption activity could indicate higher sediment production, increasing the likelihood for sliding. Slope failure can also depressurize the volcanic edifice allowing for magma to reach the surface more easily (Masson et al., 2006). But these hydroacoustic episodes lack the interference patterns expected with volcanic activity at West Mata summit suggesting either a collection of noise from a variety of sources or these signals are coming from a place other than the summit. Because of this, no concrete connection can be made between the volcanic eruption and the occurrence of landslides.

Submarine landslides have also been found to be caused by seismic activity (Masson et al., 2006). Earthquakes are marked by short duration, high amplitude hydroacoustic signals with frequencies < 100 Hz. Although the West Mata hydroacoustic record is riddled with earthquakes of variable magnitudes, it is difficult to correlate these two processes. It is often

unclear whether seismic activity is local or regional, as SOFAR moored hydrophones can pick up long range signals. Because earthquake locations are unknown it is impossible to constrain magnitude or how strongly the earthquake may have shaken the volcano. T-phase amplitudes can be used to estimate earthquake magnitude, but it is unclear how much shaking is required to produce submarine slope failures (Johnson and Northrop, 1966; Dziak, 2001). Not enough evidence exists to determine a clear relationship between these landslides and seismic activity. What is clear is that earthquakes do not occur before every slide, and the majority of landslide signals are not preceded by seismic activity.

Landslides can also result from over steepening by sediment accumulation. (Caplan-Auerbach et al., 2001; Acocella, 2005; Chadwick et al., 2008; 2012). The smooth slopes of West Mata suggest thick sediment accumulation by means of consistent gravitational settling. The western face appears smooth, which is consistent with a slope comprised of fragmental pyroclastics. At Monowai volcano, sediment accumulations downslope from collapses lack hummocks or levees and are generally smooth, which is only possible if fragmental pyroclastics are being mobilized (Chadwick et al., 2008). Broadband hydroacoustic signals at West Mata are interpreted as the chaotic flow of pyroclastic fragments, similar to the process at Monowai volcano. In this case, the process is not considered a "slide" in the classic sense where a coherent block of rock is moving down the slope on a failure plane. Rather, the term "landslide" is used loosely by referring to the mobilization of fragmental pyroclastic material down slope, losing energy with distance as is the case with a debris avalanche (Masson et al., 2006). Average velocity calculations are affected by this slow down and may not capture the top speed of West Mata slope failures. Theoretically, calculating slide velocity during the greatest change in frequency banding would result in the top speed for that particular

landslide. However, small changes in speed are not discernable given the uncertainty in modeling (+/- 20 m between source depths that change the spectral banding pattern). In comparison with landslides studied by Ward and Day (2001) West Mata slides appear overall slower. However, other limitations to their velocity formula exists. Ward and Day assume a block slide, which helps to constrain slide length (L_c). At West Mata, it's likely that fragmental material is cascading down the slopes which differs in terms of mass, velocity, and momentum.

The PIII region identified by Embley et al., (2014) is thought to represent sediment accumulation resulting from the volcanic output of West Mata. The additional zone of accumulation downslope of PIII (~1900 m – 2100 m depth, Figure 16) was inferred to be mass wasted material funneled downslope by local topography. Localized mass wasting deposits in the PIII region is consistent with experimental observations of slope failure by sediment accumulation (Acocella, 2005). The upper reaches of West Mata are sloping near the angle of repose requiring only minimal loading to trigger slope failure (Embley et al., 2014). Constant tephra output would likely trigger many slope failures over the long term. It should be noted, however, that if slope failures were occurring in the PIII region, there should be a zone of sediment deficit comparable in size to the zone of sediment accumulation. But this is not apparent in the Embley et al., 2014 investigation. Perhaps more material is accumulating in PIII than is failing, which would only display a positive depth change in this region.

5.3. Landslide processes and slide clusters

Landslides at West Mata tend to occur around the same depth (~1550 m) within the PIII region and cluster during periods of high background hydroacoustic activity. It is possible that voids caused by previous mass wasting provide grounds for sequential slope failures (Chadwick et al., 2008; Masson et al., 2006). On the Canary Islands, voids, or scars, trap sediment produced by volcanic eruptions which creates local instability, increasing the likelihood for sliding (Masson et al., 2006). Acocella (2005) experimentally showed that sequential sliding tended to occur either within these voids or along the boundaries, which act to guide the sliding material. Freshly deposited sediment from a slope failure can act as a weak layer, which also increases the likelihood for more slides (Masson et al., 2006). Landslide clusters at West Mata are consistent with this process. Sediment from West Mata eruptions likely get trapped within these voids, leading to repeated failure at a common area and depth. Pre-existing topographic channels could aide in the transport of the PIII eruptive material downslope (Embley et al., 2014).

Modeling slide clusters also revealed a pattern of decreasing run out distances throughout the day (Figure 29). Run out distance reduction suggests a decrease in sediment volume, or decrease in local slope with each successive failure. Correlating run out distance with slide velocity throughout each day did not reveal a true reason for the reduction in run out distance. Less striking is the observation of decreasing failure depth throughout the day. However, the hydroacoustic model used in this study may not be precise enough to reveal a true pattern of failure and with no way to locate the events on a map, this is approach is additionally challenging.

VI. CONCLUSIONS

The eruption of West Mata represents only the second time active submarine volcanism has been observed. Hydroacoustic monitoring allowed for clear recording of dynamic eruption processes and frequent submarine landslides. This study explored the detail to which these submarine landslides could be modeled using the principles of interference by multipath rays. Hydroacoustic modeling revealed that during a 5-month eruptive period, landslides frequently bombarded the western flank, 200-300 m below the Hades eruptive vent, traveling between 4-8 m/s on average with speeds possibly reaching 20 m/s. Slides on West Mata are suggested to be caused by the unstable loading of tephra near sites of previous mass wasting during periods of high intensity eruptions. Landslides also tend to cluster with some days producing >35 events. Run out distances tend to decrease over the course of a cluster suggesting either a decrease in slide volume or local slope. Seismic shaking may influence when these landslides occur, although no evidence suggests that this is always the case. West Mata represents a well recorded relationship between active volcanism and frequent submarine landslides that together are critical processes in the development of submarine volcanoes.

VII. REFERENCES

Acocella, V., 2005, Modes of sector collapse of volcanic cones: Insights from analogue experiments: ANALOGUE MODELS OF VOLCANO COLLAPSE: Journal of Geophysical Research: Solid Earth, v. 110, doi: 10.1029/2004JB003166.

Baumberger, T., Lilley, M.D., Resing, J.A., Lupton, J.E., Baker, E.T., Butterfield, D.A., Olson, E.J., and Früh-Green, G.L., 2014, Understanding a submarine eruption through time series hydrothermal plume sampling of dissolved and particulate constituents: West Mata, 2008–2012: Geochemistry, Geophysics, Geosystems, v. 15, p. 4631–4650, doi: 10.1002/2014GC005460.

Caplan-Auerbach, J., Chadwick, W.W., Lau, T.K., Bohnensteihl, D., and Dziak, R.P., 2014, Analysis of Submarine Landslides at West Mata Volcano, NE Lau Basin, Using Hydroacoustic Data:

Caplan-Auerbach, J., Dziak, R.P., Bohnenstiehl, D.R., Chadwick, W.W., and Lau, T.-K., 2014, Hydroacoustic investigation of submarine landslides at West Mata volcano, Lau Basin: LANDSLIDES AT WEST MATA VOLCANO: Geophysical Research Letters, v. 41, p. 5927–5934, doi: 10.1002/2014GL060964.

Caplan-Auerbach, J., Fox, C.G., and Duennebier, F.K., 2001, Hydroacoustic detection of submarine landslides on Kilauea volcano: Geophysical Research Letters, v. 28, p. 1811.

Chadwick, W.W., Dziak, R.P., Haxel, J.H., Embley, R.W., and Matsumoto, H., 2012, Submarine landslide triggered by volcanic eruption recorded by in situ hydrophone: Geology, v. 40, p. 51–54, doi: 10.1130/G32495.1.

Chadwick, W.W., Wright, I.C., Schwarz-Schampera, U., Hyvernaud, O., Reymond, D., and de Ronde, C.E.J., 2008, Cyclic eruptions and sector collapses at Monowai submarine volcano, Kermadec arc: 1998–2007: Geochemistry, Geophysics, Geosystems, v. 9, p. Q10014, doi: 10.1029/2008GC002113.

Clague, D.A., Paduan, J.B., Caress, D.W., Thomas, H., Chadwick, W.W., and Merle, S.G., 2011, Volcanic morphology of West Mata Volcano, NE Lau Basin, based on high-resolution bathymetry and depth changes: Geochemistry, Geophysics, Geosystems, v. 12, http://onlinelibrary.wiley.com/doi/10.1029/2011GC003791/pdf (accessed October 2015).

Dziak, R.P., 2001, Empirical relationship of T-wave energy and fault parameters of northeast Pacific Ocean earthquakes: Geophysical Research Letters, v. 28, p. 2537–2540, doi: 10.1029/2001GL012939.

Dziak, R.P., Bohnenstiehl, D.R., Baker, E.T., Matsumoto, H., Caplan-Auerbach, J., Embley, R.W., Merle, S.G., Walker, S.L., Lau, T.-K., and Chadwick, W.W., 2015, Long-term explosive degassing and debris flow activity at West Mata submarine volcano: Geophysical Research Letters, v. 42, p. 1480–1487, doi: 10.1002/2014GL062603.

Embley, R.W., Merle, S.G., Baker, E.T., Rubin, K.H., Lupton, J.E., Resing, J.A., Dziak, R.P., Lilley, M.D., Chadwick, W.W., Shank, T., Greene, R., Walker, S.L., Haxel, J., Olson, E., et al., 2014, Eruptive modes and hiatus of volcanism at West Mata seamount, NE Lau basin: 1996-2012: Geochemistry, Geophysics, Geosystems, v. 15, p. 4093–4115, doi: 10.1002/2014GC005387.

Ewing, M., Tolstoy, I., and Press, F., 1950, Proposed use of the T phase in tsunami warning systems: Bulletin of the Seismological Society of America, v. 40, p. 53–58.

GeoMapApp, http://www.geomapapp.org/ (accessed January 2017).

de Groot-Hedlin, C.D., and Orcutt, J.A., 1999, Synthesis of earthquake-generated T-waves: Geophysical Research Letters, v. 26, p. 1227–1230, doi: 10.1029/1999GL900205.

Hampton, M.A., Lee, H.J., and Locat, J., 1996, Submarine landslides: Reviews of Geophysics, v. 34, p. 33–59, doi: 10.1029/95RG03287.

Johnson, R.H., and Norris, R.A., 1972, Significance of spectral banding in hydroacoustic signals from submarine volcanic eruptions: Myojin, 1970: Journal of Geophysical Research, v. 77, p. 4461–4469, doi: 10.1029/JB077i023p04461.

Johnson, R.H., and Northrop, J., 1966, A comparison of earthquake magnitude with T-phase strength: Bulletin of the Seismological Society of America, v. 56, p. 119–124.

Johnson, R, H., J. Northrop, and R. Eppley, 1963, Sources of Pacific T Phases: Journal of Geophysical Research, v. 68, p. 4251–4260.

Krastel, S., Schmincke, H.-U., Jacobs, C.L., Rihm, R., Le Bas, T.P., and Alibés, B., 2001, Submarine landslides around the Canary Islands: Journal of Geophysical Research: Solid Earth, v. 106, p. 3977–3997, doi: 10.1029/2000JB900413.

Kuroda, N., Shiraki, K., and Urano, H., 1978, Boninite as a possible calc-alkalic primary magma: Bulletin Volcanologique, v. 41, p. 563–575, doi: 10.1007/BF02597387.

Mack, C.J., 2014, Quantifying submarine eruptive flux from interpretation of hydroacoustic signals, West Mata Volcano, Lau Basin:, http://cedar.wwu.edu/wwuet/378/ (accessed March 2017).

Masson, D.G., Harbitz, C.B., Wynn, R.B., Pedersen, G., and Lovholt, F., 2006, Submarine landslides: processes, triggers and hazard prediction: Philosophical Transactions of the Royal Society A: Mathematical, Physical and Engineering Sciences, v. 364, p. 2009–2039, doi: 10.1098/rsta.2006.1810.

Matsumoto, H., Haxel, J.H., Dziak, R.P., Bohnenstiehl, D.R., and Embley, R.W., 2011, Mapping the sound field of an erupting submarine volcano using an acoustic glider: The Journal of the Acoustical Society of America, v. 129, p. EL94–EL99.

Merle, S., 2009, NE Lau Basin Response Cruise Report:

Okal, E.A. T Waves: Encyclopedia of Solid Earth Geophysics, p. 1421–1423.

Okal, E.A., 2003, T Waves from the 1998 Papua New Guinea Earthquake and its Aftershocks: Timing the Tsunamigenic Slump: Pure and Applied Geophysics, v. 160, p. 1843–1863, doi: 10.1007/s00024-003-2409-x.

Okal, E.A., 2001, T-phase stations for the International Monitoring System of the Comprehensive Nuclear-Test Ban Treaty: A global perspective: Seismological Research Letters, v. 72, p. 186–196.

Porter, M.B., 2011, The bellhop manual and user's guide: Preliminary draft: Heat, Light, and Sound Research, Inc., La Jolla, CA, USA, Tech. Rep, http://oalib.hlsresearch.com/Rays/HLS-2010-1.pdf (accessed January 2017).

Pulli, J.J., and Upton, Z.M., 2002, Hydroacoustic observations of Indian earthquake provide new data on T-waves: Eos, Transactions American Geophysical Union, v. 83, p. 145–151, doi: 10.1029/2002EO000090.

Resing, J.A., Rubin, K.H., Embley, R.W., Lupton, J.E., Baker, E.T., Dziak, R.P., Baumberger, T., Lilley, M.D., Huber, J.A., Shank, T.M., Butterfield, D.A., Clague, D.A., Keller, N.S., Merle, S.G., et al., 2011, Active submarine eruption of boninite in the northeastern Lau Basin: Nature Geoscience, v. 4, p. 799–806, doi: 10.1038/ngeo1275.

Ryan, W.B.F., Carbotte, S.M., Coplan, J.O., O'Hara, S., Melkonian, A., Arko, R., Weissel, R.A., Ferrini, V., Goodwillie, A., Nitsche, F., Bonczkowski, J., and Zemsky, R., 2009, Global Multi-Resolution Topography synthesis: Geochemistry, Geophysics, Geosystems, v. 10, p. Q03014, doi: 10.1029/2008GC002332.

Tenzer, R., and Gladkikh, V., 2014, Assessment of Density Variations of Marine Sediments with Ocean and Sediment Depths: The Scientific World Journal, v. 2014, p. e823296, doi: 10.1155/2014/823296.

Ward, S.N., and Day, S., 2002, Suboceanic landslides: 2002 Yearbook of Science and Technology, p. 349–352.

Wilson, J.K., 2007, Maritime surveillance using a wideband hydrophone: Monterey, California. Naval Postgraduate School, http://calhoun.nps.edu/handle/10945/3214 (accessed May 2017).

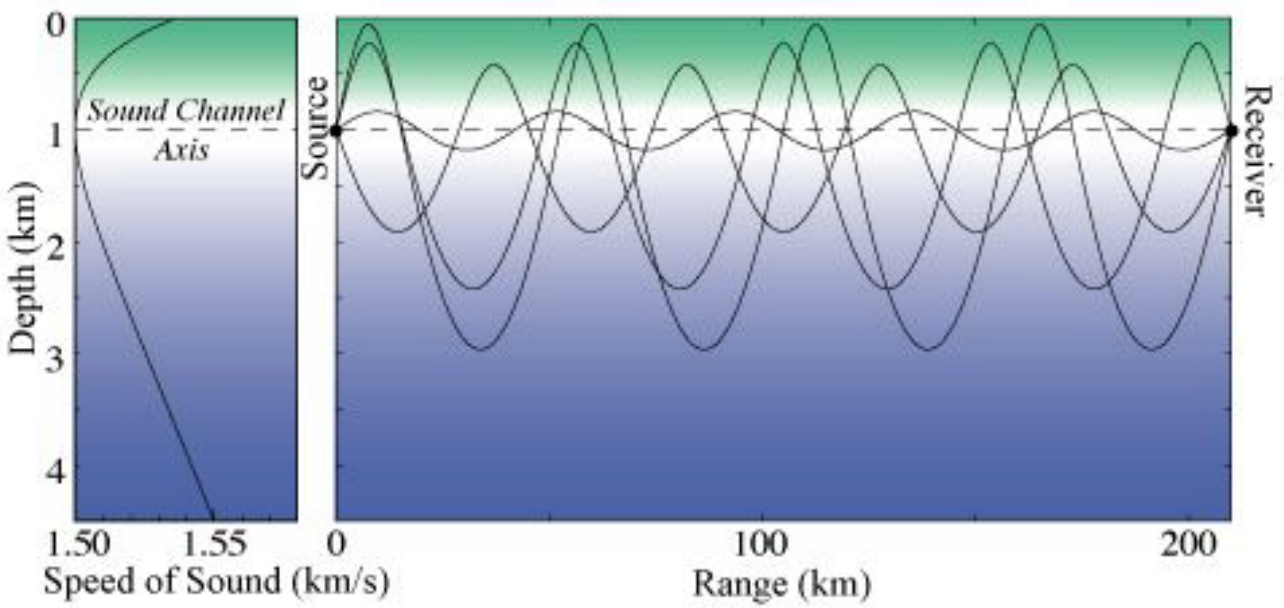

Fig. 1. SOFAR channel illustration. Sound waves tend to bend toward a region of low velocity within the world's oceans. They become trapped within this channel and travel thousands of kilometers with minimal attenuation. Figure from "Discovery of Sound in the Sea" website (www.dosits.org).

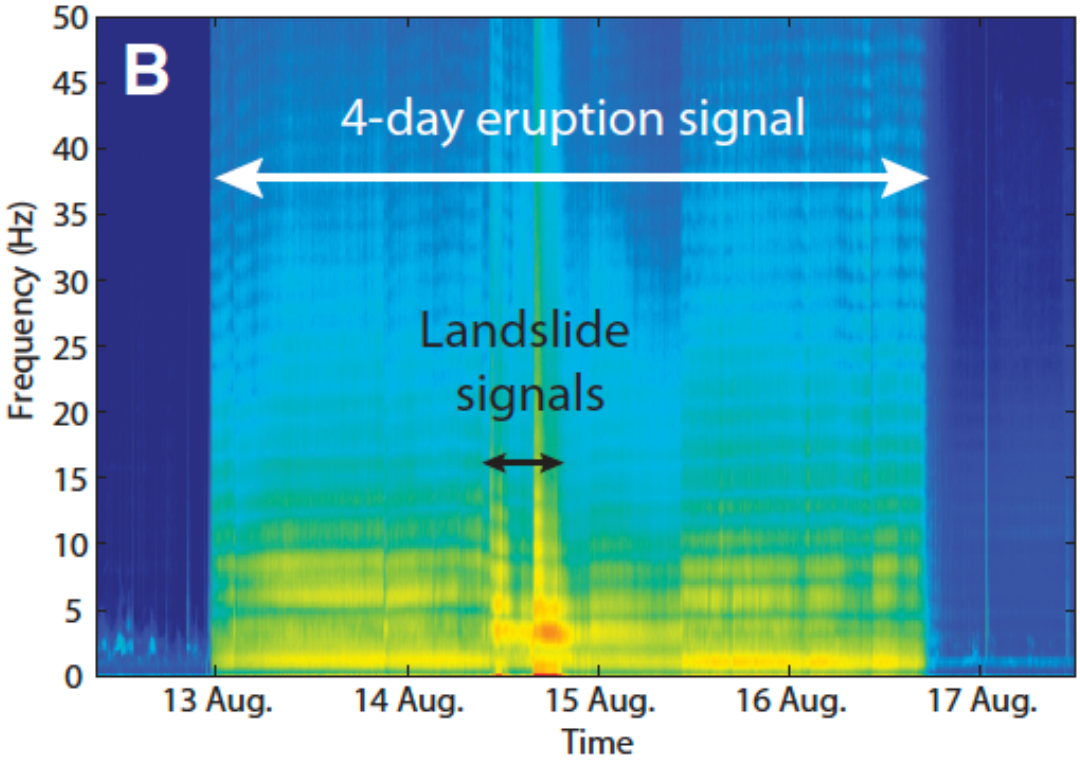

Fig. 2. Landslide signals during high intensity volcanic eruption at NW-Rota-1 (Chadwick et al., 2012). These landslide signals are interpreted as a series of smaller landslides occurring during overall high background hydroacoustic activity.

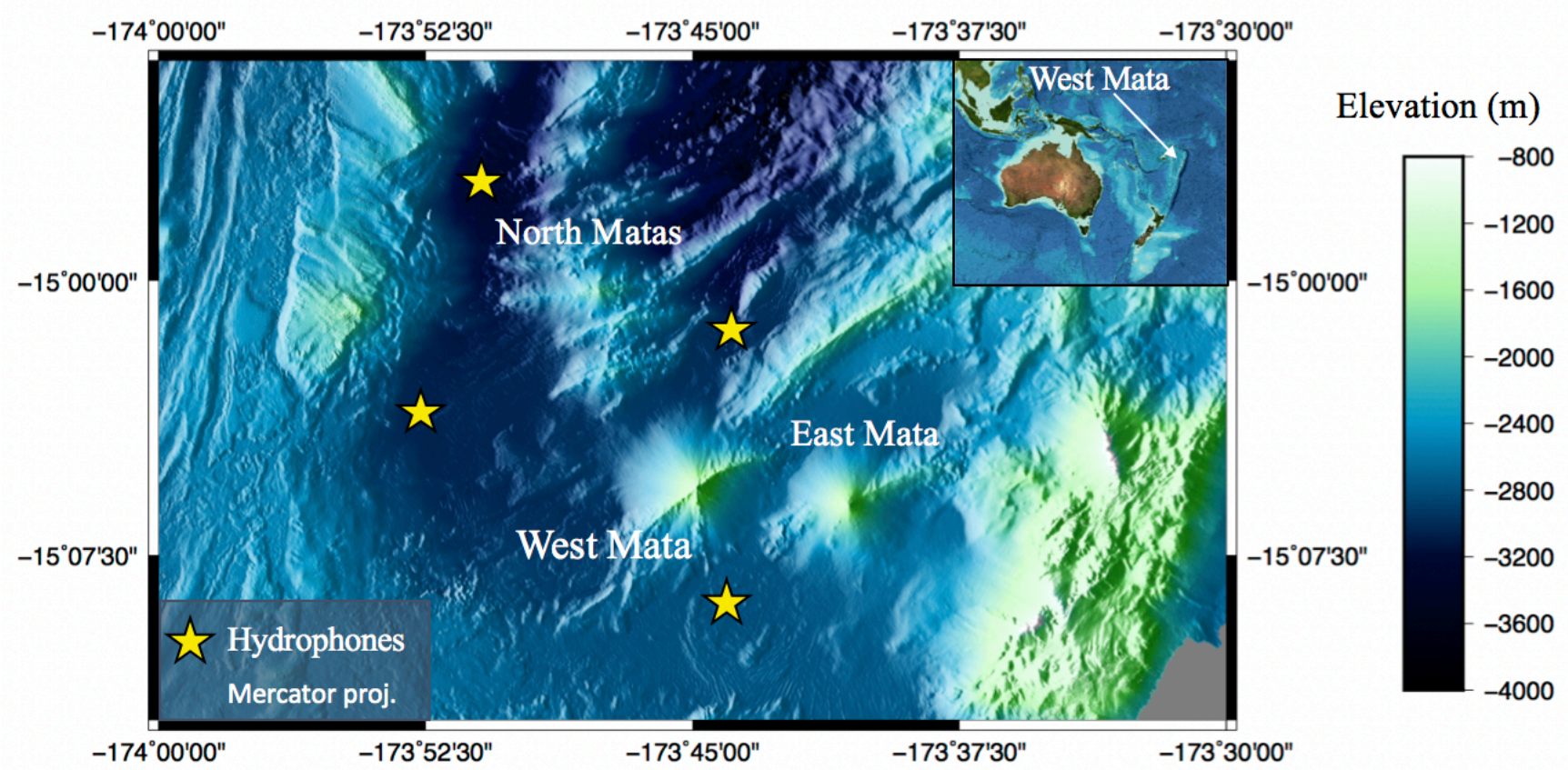

Fig. 3. West Mata is part of a complex of elongate volcanoes in the NE Lau Basin. The yellow stars indicate the locations of the hydrophones used for this investigation. The inset figure is a smaller scale representation of West Mata in the Tonga arc, east of Australia and north of New Zealand. Each border segment length is about 12.5 km. Bathymetric grid (100 m) curtesy of Susan Merle, NOAA.

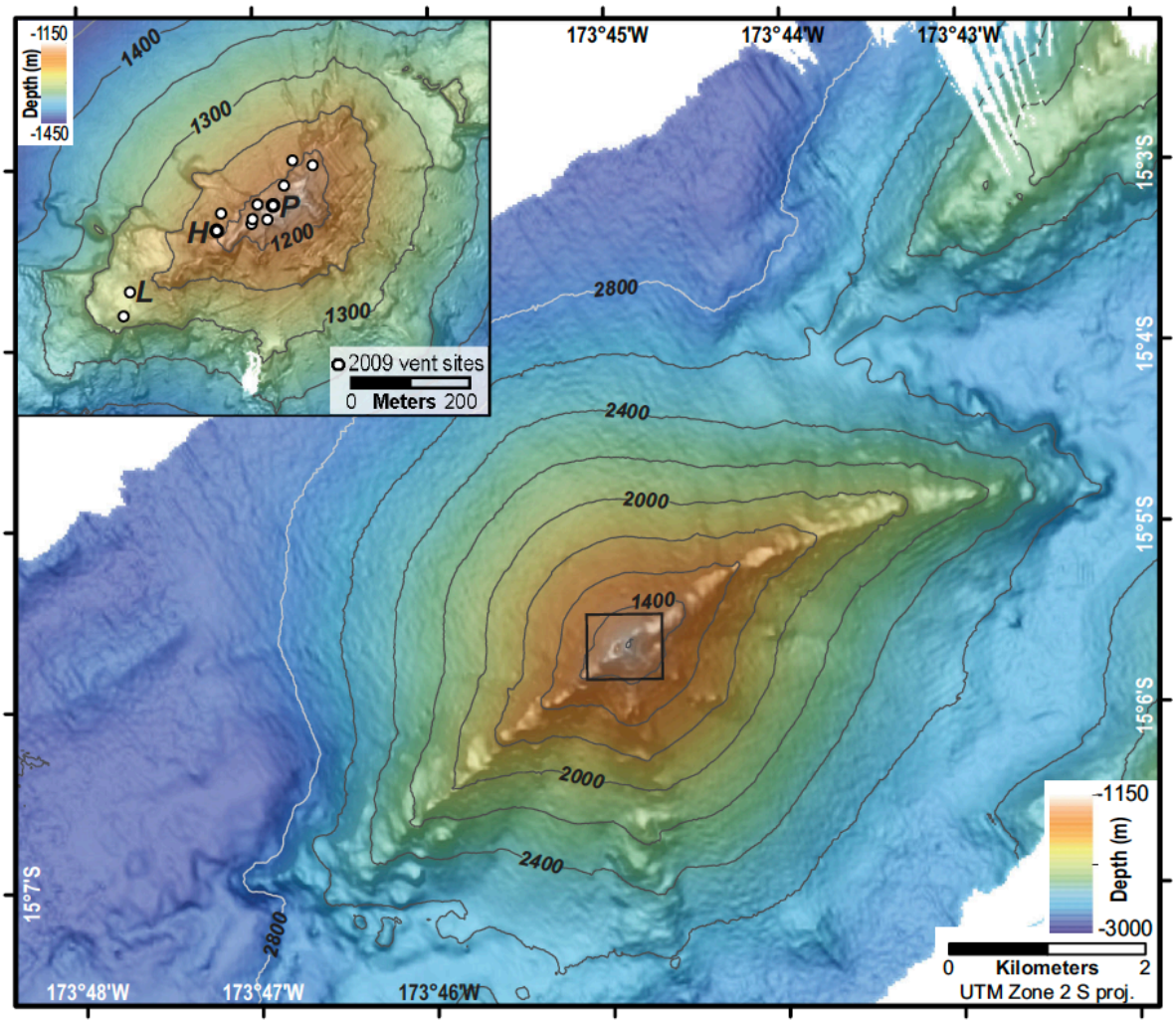

Fig. 4. High resolution (20 m grid size) bathymetry of West Mata (figure from Embley et al., 2014). Inset image shows eruptive vents Hades (H) and Prometheus (P), and Luo (L) as well as other eruptive and hydrothermal vents (white circles). High resolution bathymetry data collected by EM122 multibeam system on the *R/V Kilo Moana* in 2011. Underlying bathymetry data collected by multibeam sonar on the MBARI *D. Allan B. AUV* (Clague et al., 2011).

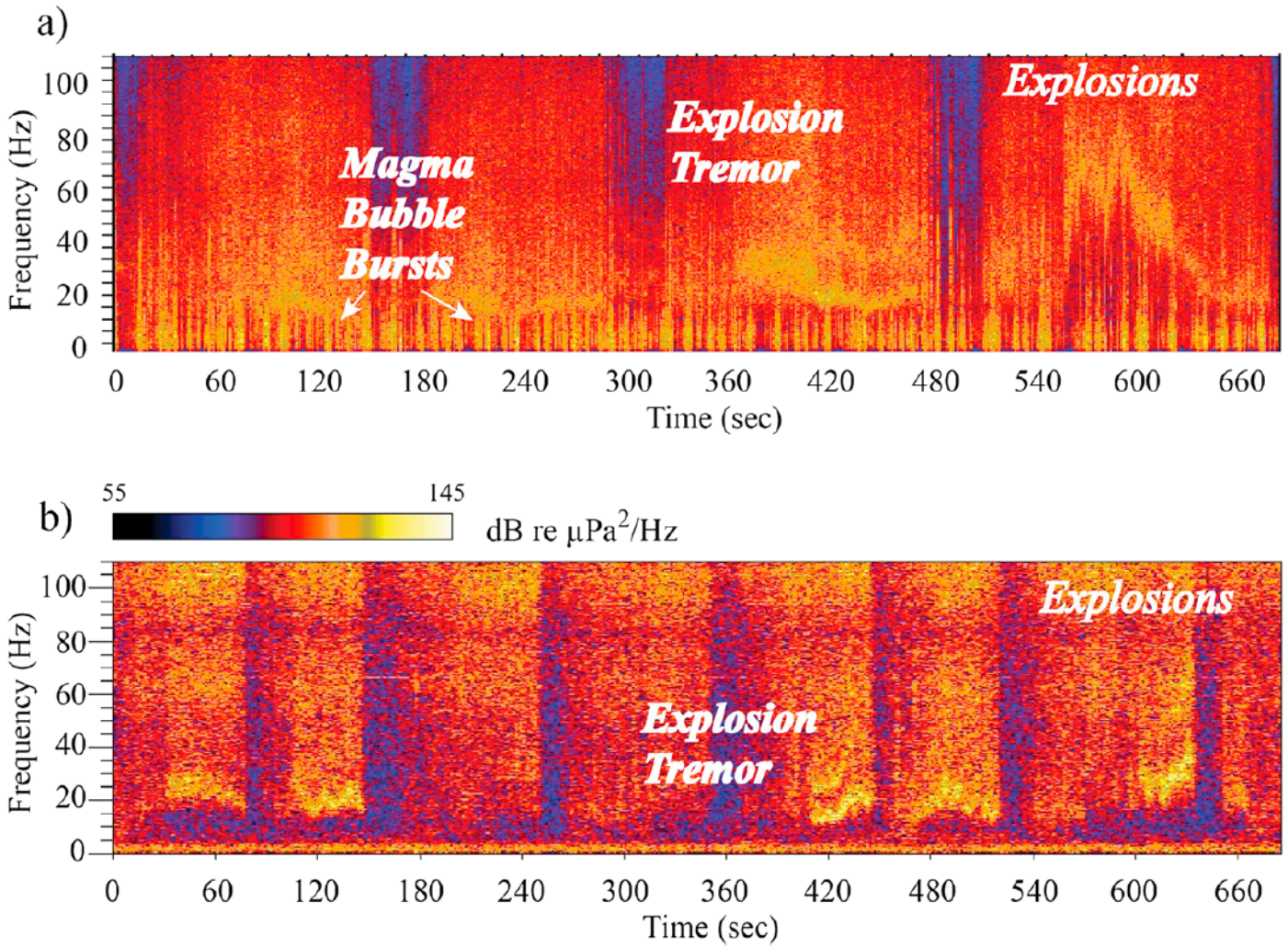

Fig. 5. Spectral character for common volcanic processes of West Mata (figure from Dziak et al., 2015). Bright colors represent high intensity activity while dark blue represents relative quiescence. Magma bubble bursts are short low frequency pulses and explosion tremors are longer broadband signals. Diffuse signals end abruptly suggesting the formation of a magma quench cap (Mack, 2014).

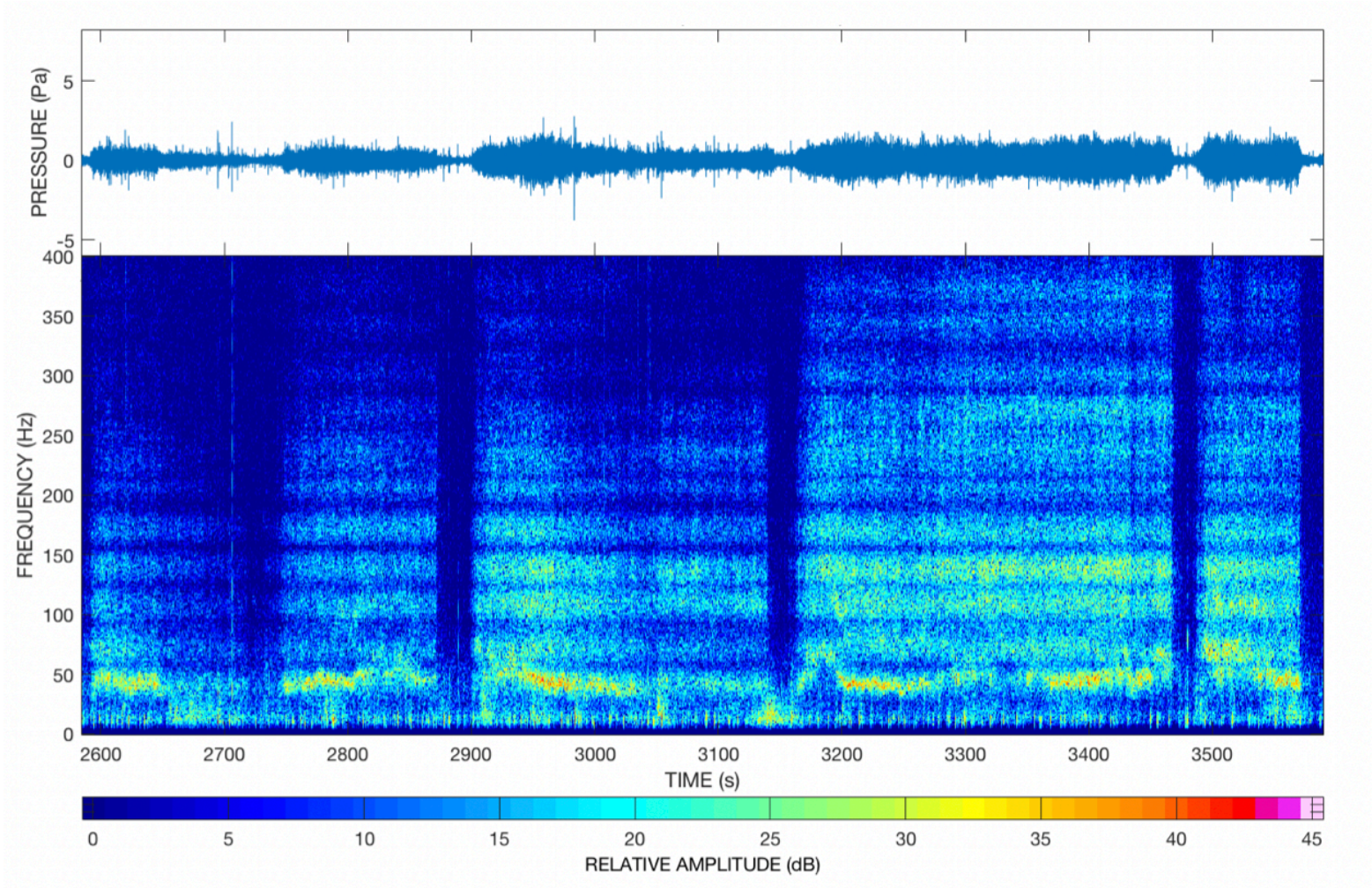

Fig. 6. Sample spectrogram from the north hydrophone. Sample displays time (seconds) on the x-axis, frequency (Hz) on the y-axis. Bright colors indicate a stronger relative signal; dark colors represent quiet signal. The time series is plotted above the spectrogram. A high pass filter (cutoff = 10 Hz) was applied here to limit the influence of low frequency noise. The vertical pulses here are suggested to be pulsating periods of volcanic activity (Dziak et al., 2015).

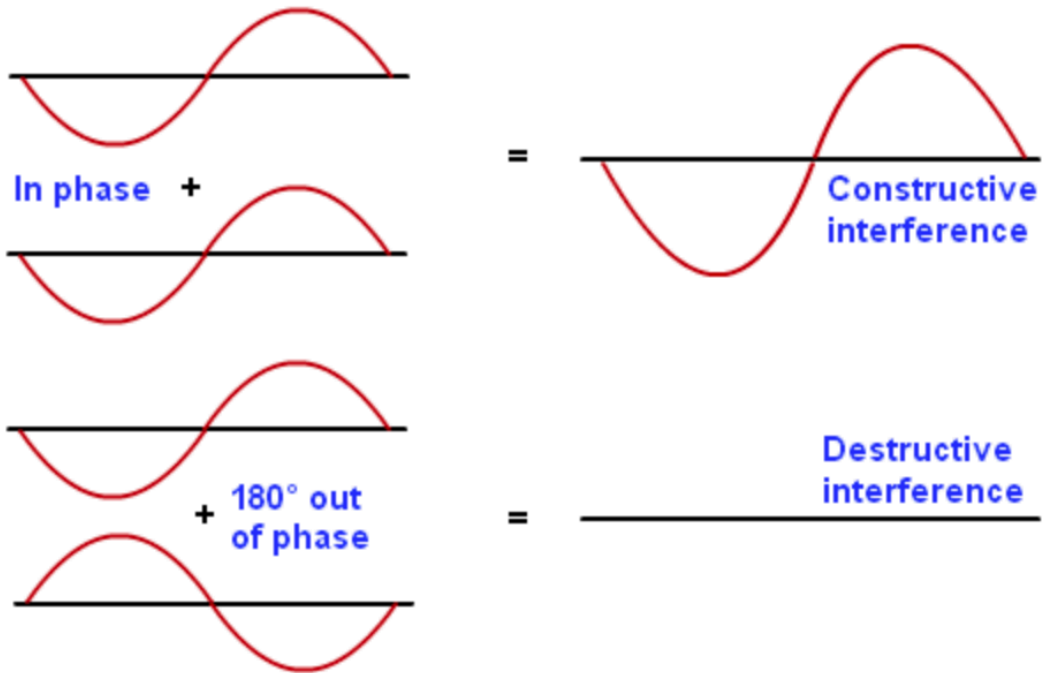

Fig. 7. Basic principles of wave interference. Waves in phase add constructively, but waves perfectly out of phase cancel one another out resulting in a quiet signal at the receiver. Interference is dependent on wavelength and phase. Image from imgarcade.com.

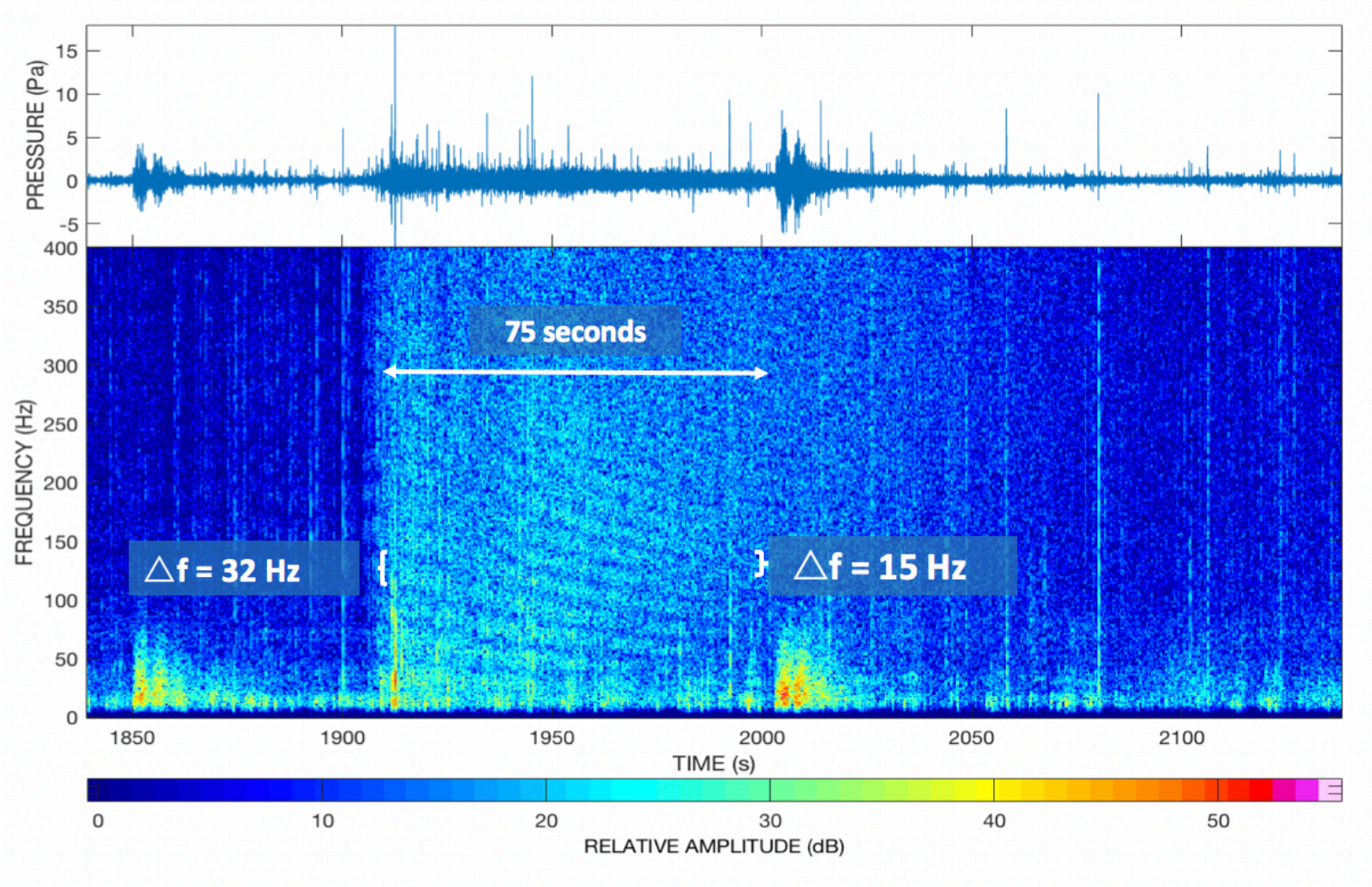

Fig. 8. Noteworthy signal recorded by the northern hydrophone. The signal is broadband and contains spectral bands that decrease in frequency with time. Spectral bands are visible for ~75 seconds until the signal blends in with background activity and the spectral bands are no longer visible. Changing interference frequencies indicates a moving source

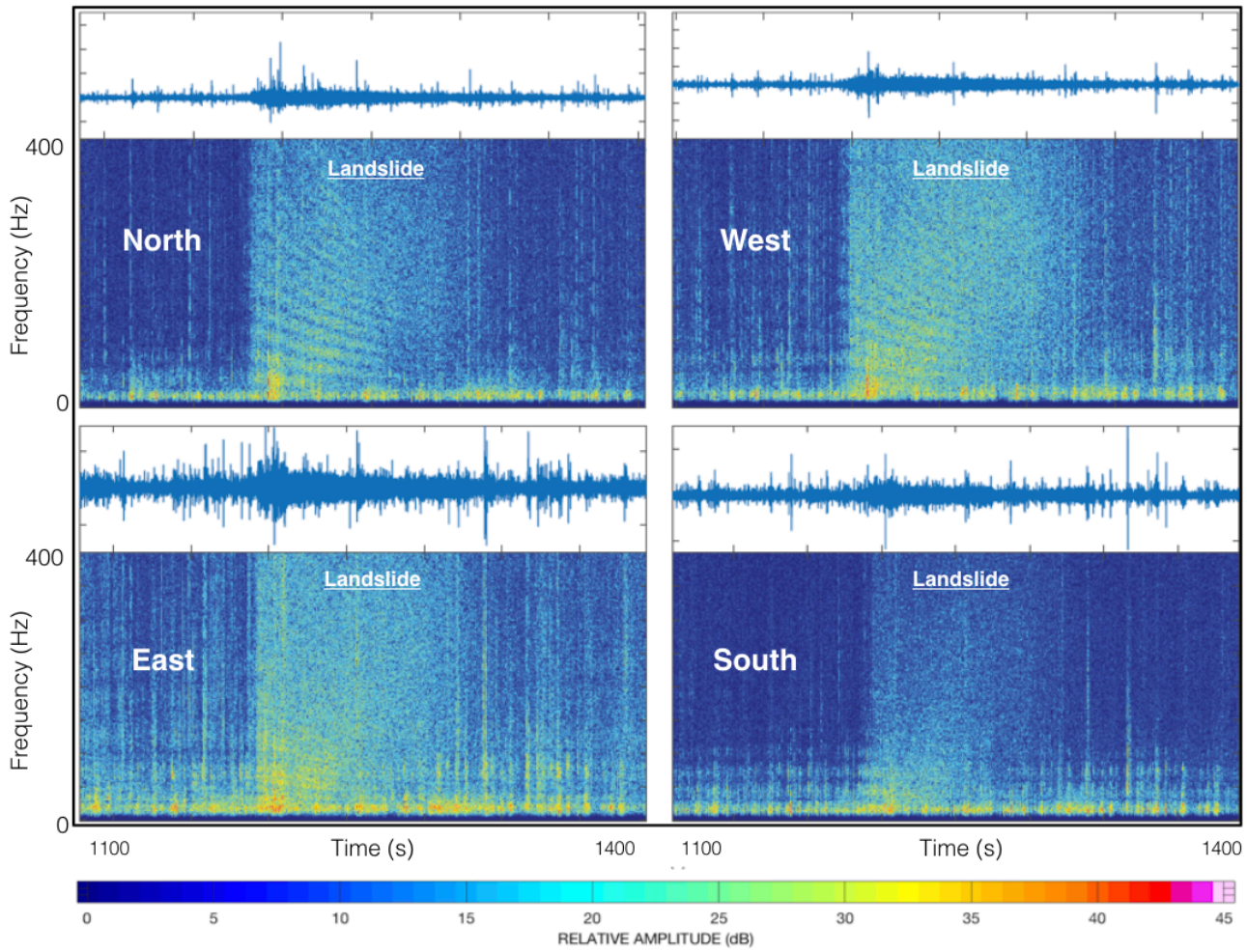

Fig. 9. Landslide captured by all four hydrophones. Only the north and west hydrophones display clear changing interference bands throughout the duration of the signal. The southern station receives the weakest overall signal relative to the other stations. The eastern and southern hydrophones display background interference from volcanic activity, but not during landslides.

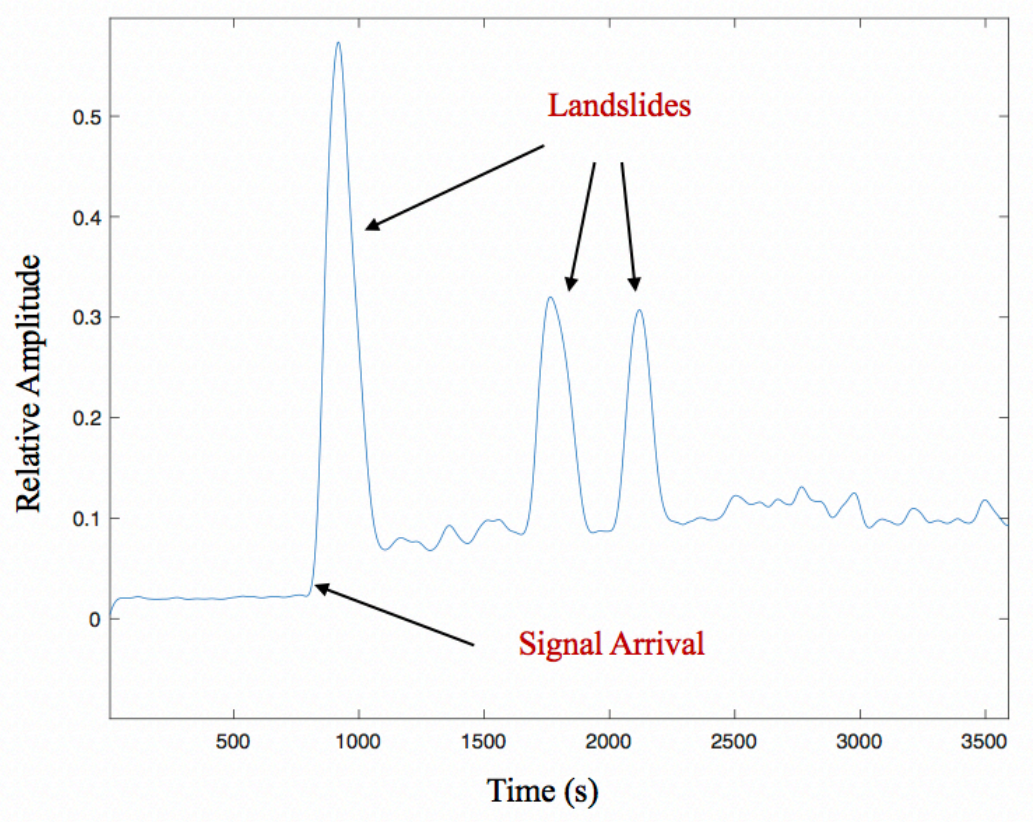

Fig. 10. Filtered data displaying signal envelopes for three separate landslides recorded by the north station. Signal envelopes were produced by first applying a high pass filter to remove low frequency noise, calculating the absolute value of the resulting waveform, and then applying a low pass filter to capture the entire landslide events. Overall background noise is higher following the initial landslide.

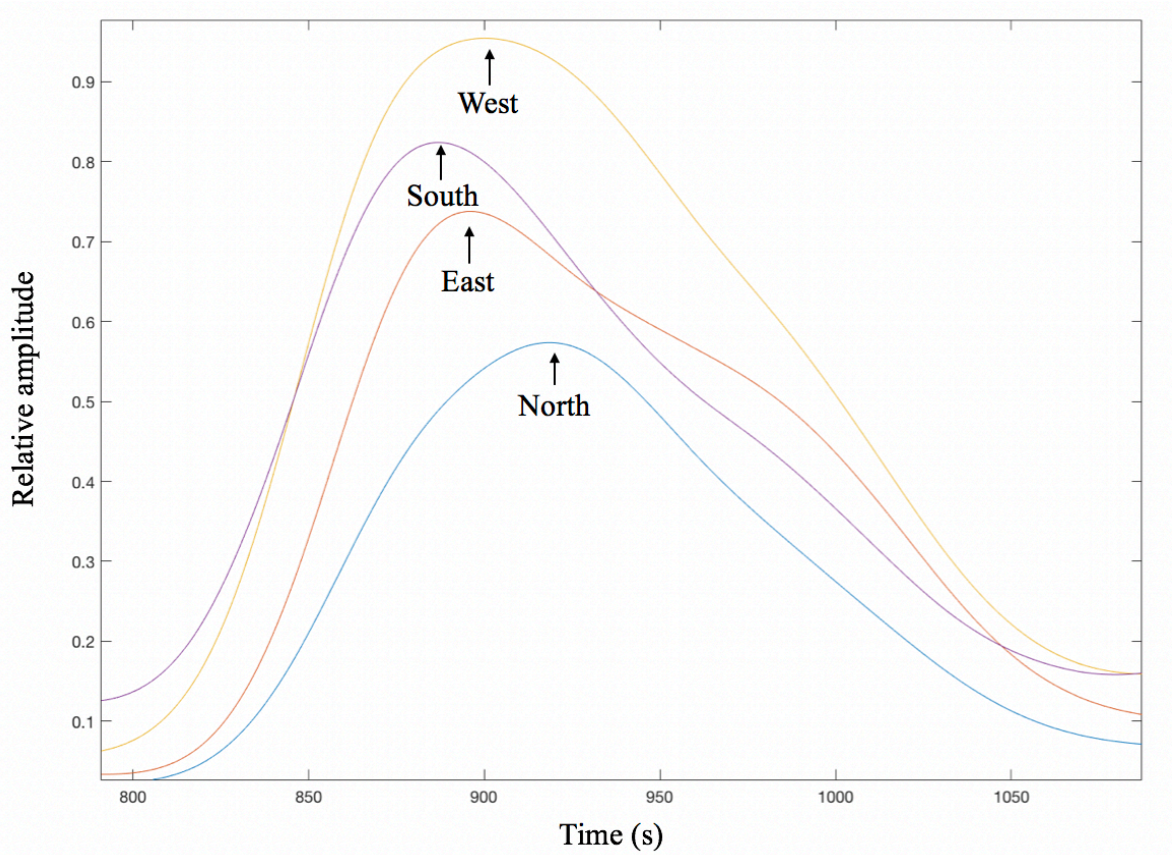

Fig. 11. Landslide signal delays for the entire array using waveform envelopes. Peak signal amplitudes were compared in this figure for easier interpretation of signal delay. Note that the southern station received a significantly weaker signal, so its amplitude was artificially increased to compare with the other stations. Signal delays are consistent with a landslide on West Mata.

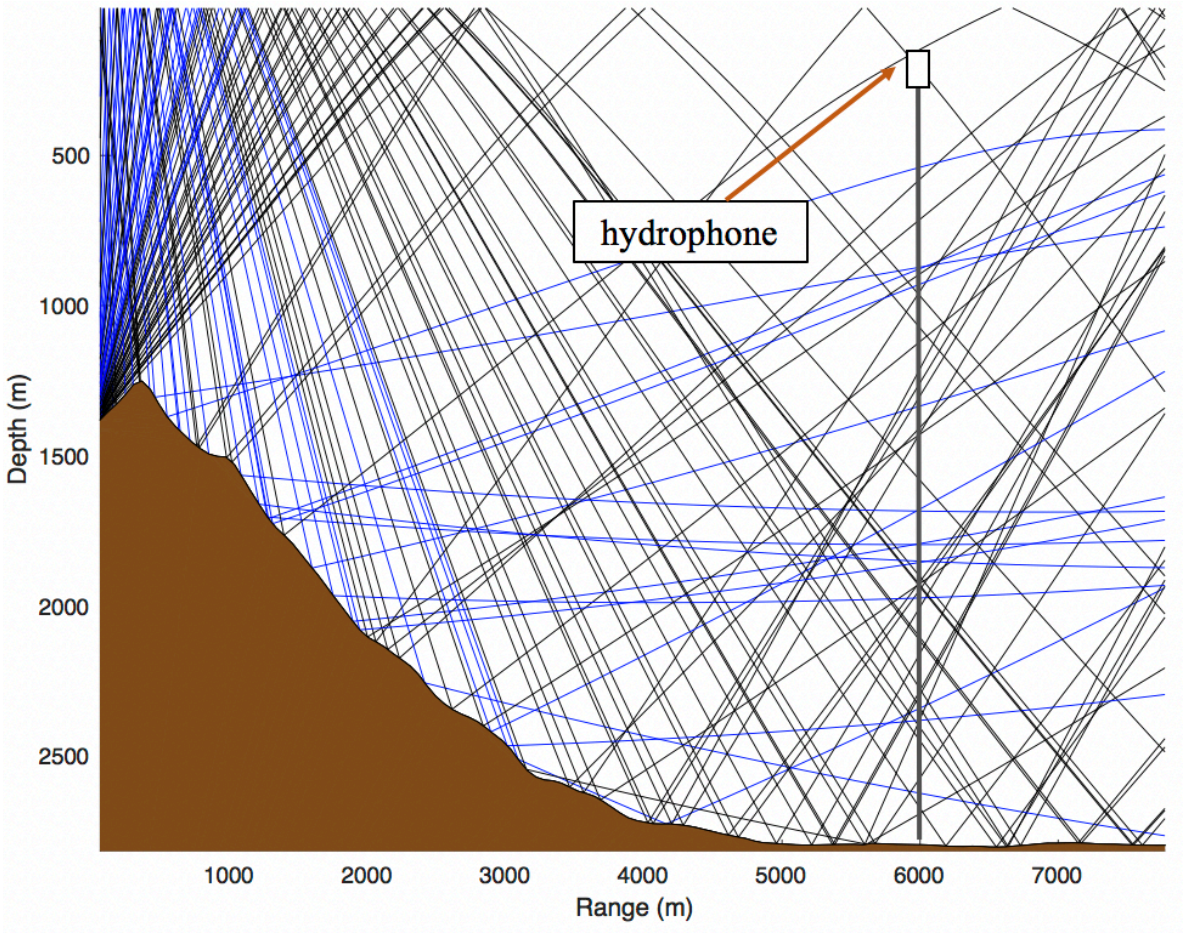

Fig. 12. Ray paths emitting from a hypothetical source on West Mata's northern flank captured by the southern hydrophone. Of the 50 rays produced, only 1 ray is captured by the hydrophone suggesting that the southern station would record signals occurring on the NW/W side of West Mata, but not clearly. Bathymetric profile is not to scale.

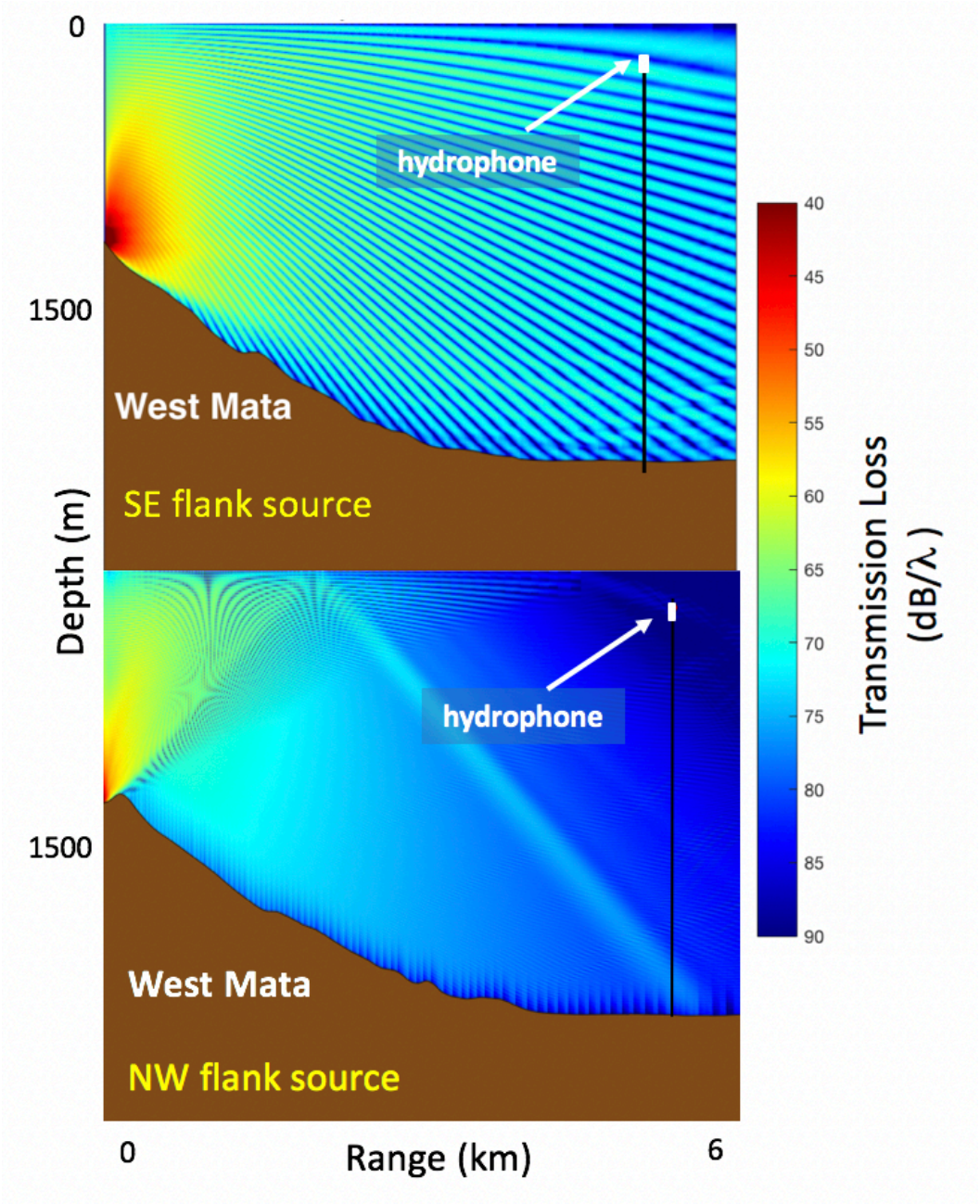

Fig. 13. A hypothetical 70 Hz sound source on the SE flank (top) and NW flank (bottom) captured by the southern hydrophone. A clear pattern of transmission loss zones are shown near the receiver with a source of the SE side. Interference bands are not observed during landslides on the southern hydrophone so they cannot be occurring on the SE side. Bathymetric profiles are not to scale.

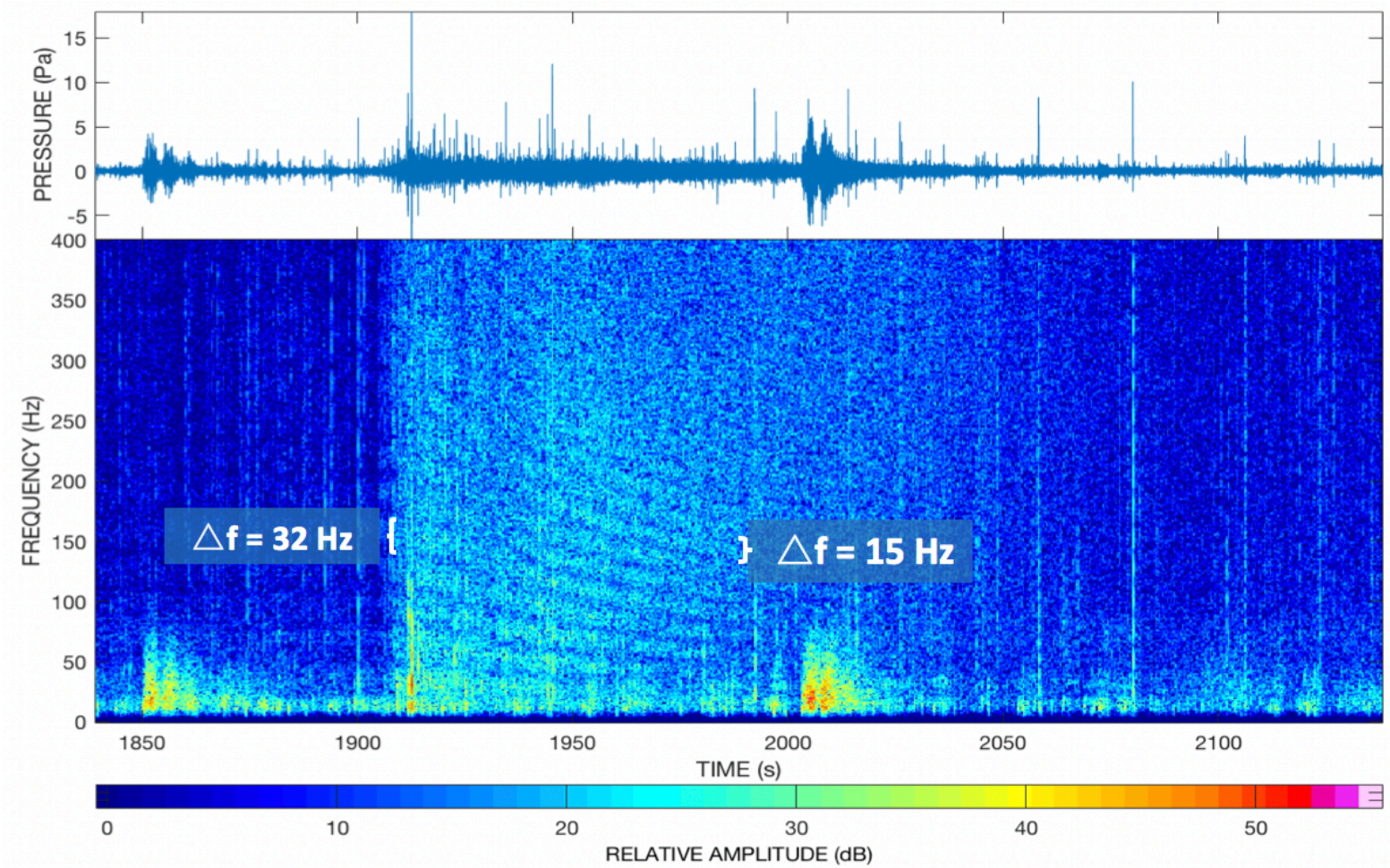

Fig. 14. Landslide signal captured on the north station. The signal is broadband with spectral bands that decrease in spacing with time. The beginning of the signal contains spectral bands spaced every ~32 Hz and ends with band spacing every ~15 Hz. These bands are overtones of the fundamental frequency.

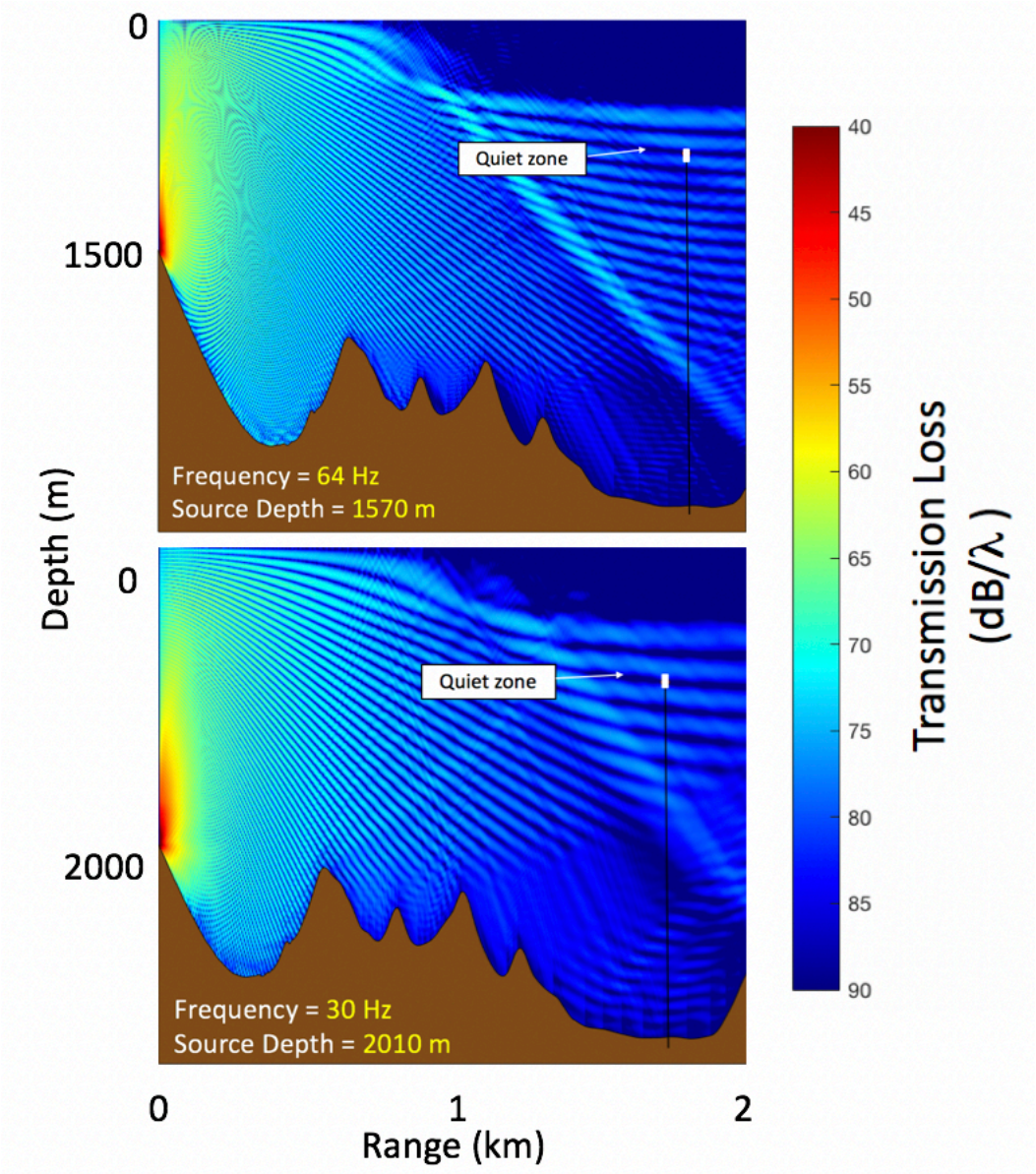

Fig. 15. Source depths tested using the second overtone of the observed spectral band spacing ($f = 2*\Delta f$) at the beginning of the landslide signal and the end of the landslide signal. Starting with the observed frequency spacing of the interference bands, source depths were tested ~40 m until the receiver was floating in a quiet zone. When the receiver is in the quiet zone, it will record a signal with frequency spacing at integer multiples of half the tested frequency. This example shows a source beginning at ~1570 m depth and traveling downslope to ~2010 m depth, based on the changing spectral band spacing on the north hydrophone.

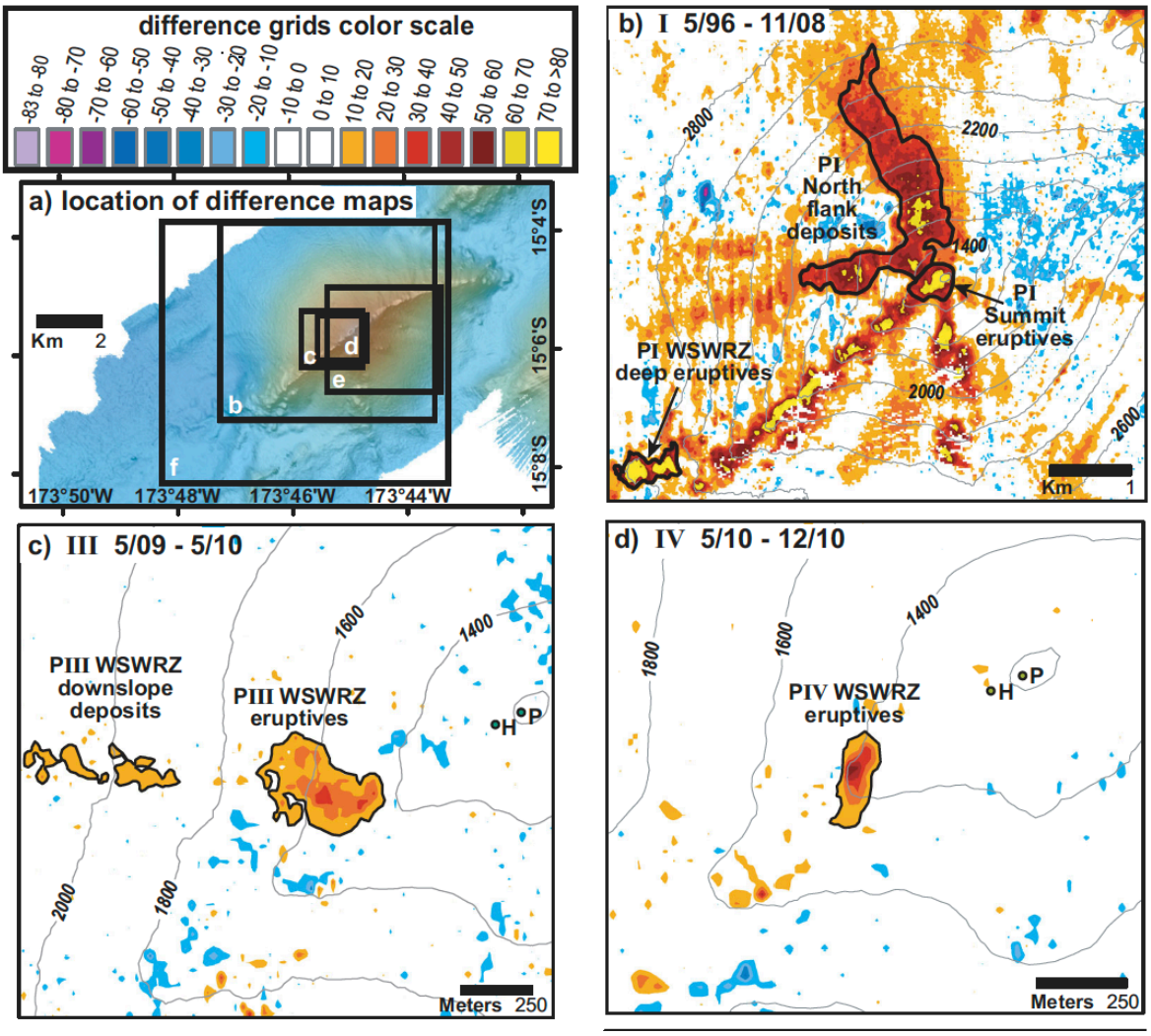

Fig. 16. Bathymetric difference maps (Modified from Embley et al., 2014). Color scale is depth in meters. Map c) displays an increase in depth during the period of hydrophone deployment for this study. PIII is interpreted as an accumulation tephra and lava from the volcanic eruption. PIII downslope deposits are interpreted as mass wasted material from the PIII upper region. Caplan-Auerbach et al. 2014 assumed the landslide origin was at the PI site, but that location is inconsistent with modeling results.

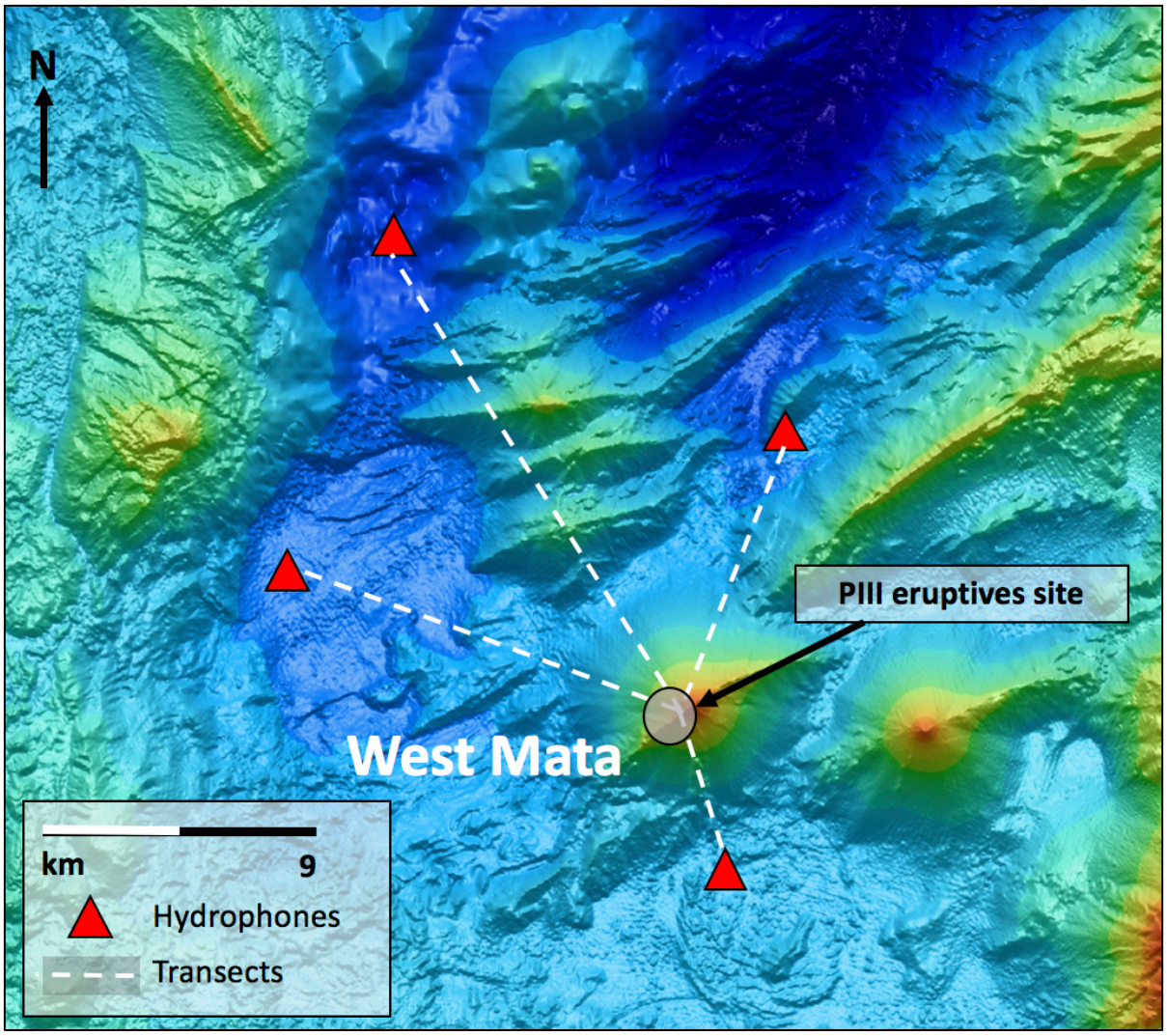

Fig. 17. Bathymetric transects used to model landslides. Transects were oriented through the PIII region on the western face of West Mata. Transects were extracted from GeoMapApp using a 100 m bathymetric grid. Figure is modified from PMEL media outlet on the NOAA ocean explorer website.

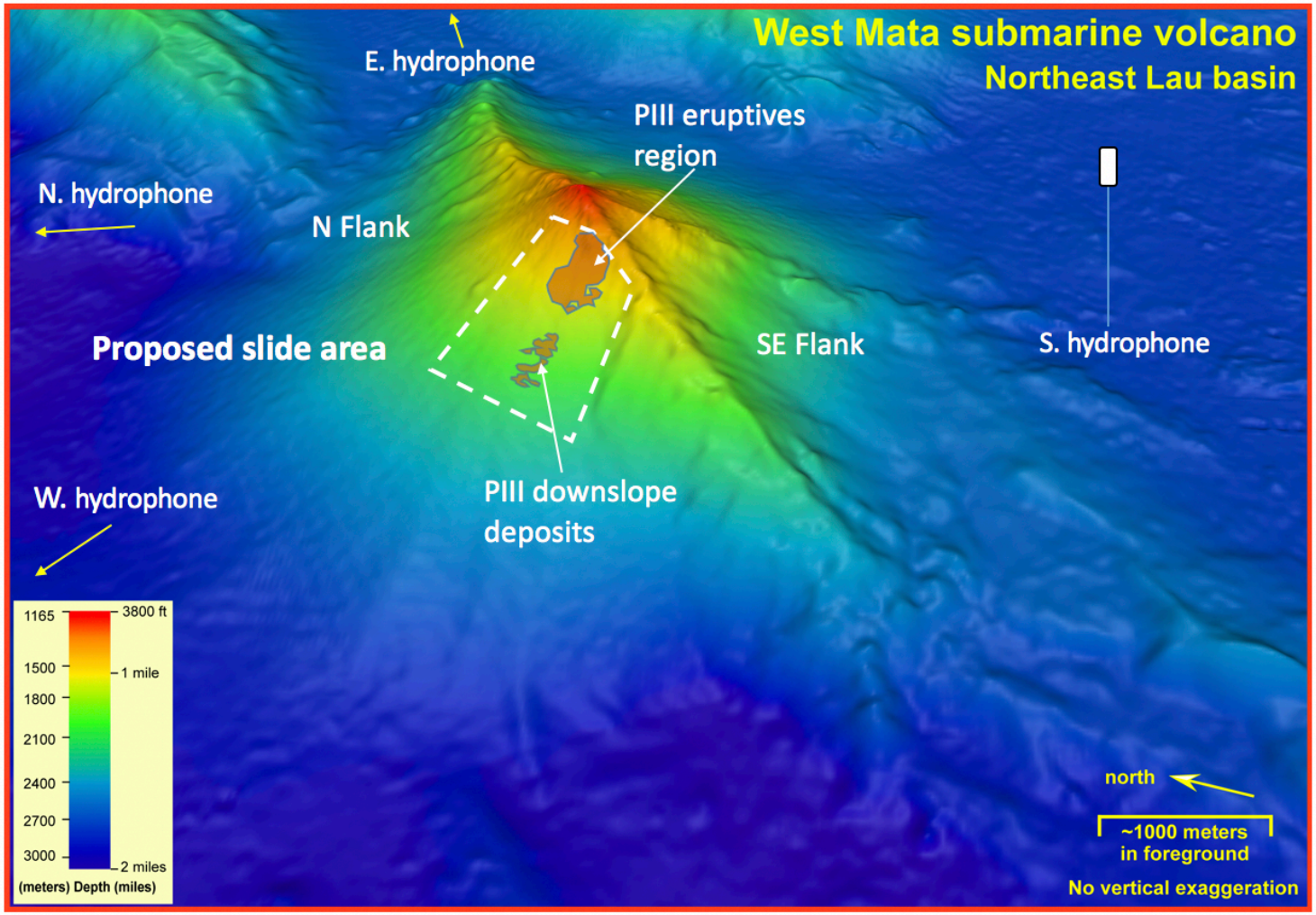

Fig. 18. Proposed slide area on the western flank of West Mata containing PIII. Landslides are suggested to occur on the western face, within the region outlined by the dashed white line. Figure is modified from NOAA, PMEL media outlet and PIII region is used from Embley et al., 2015.

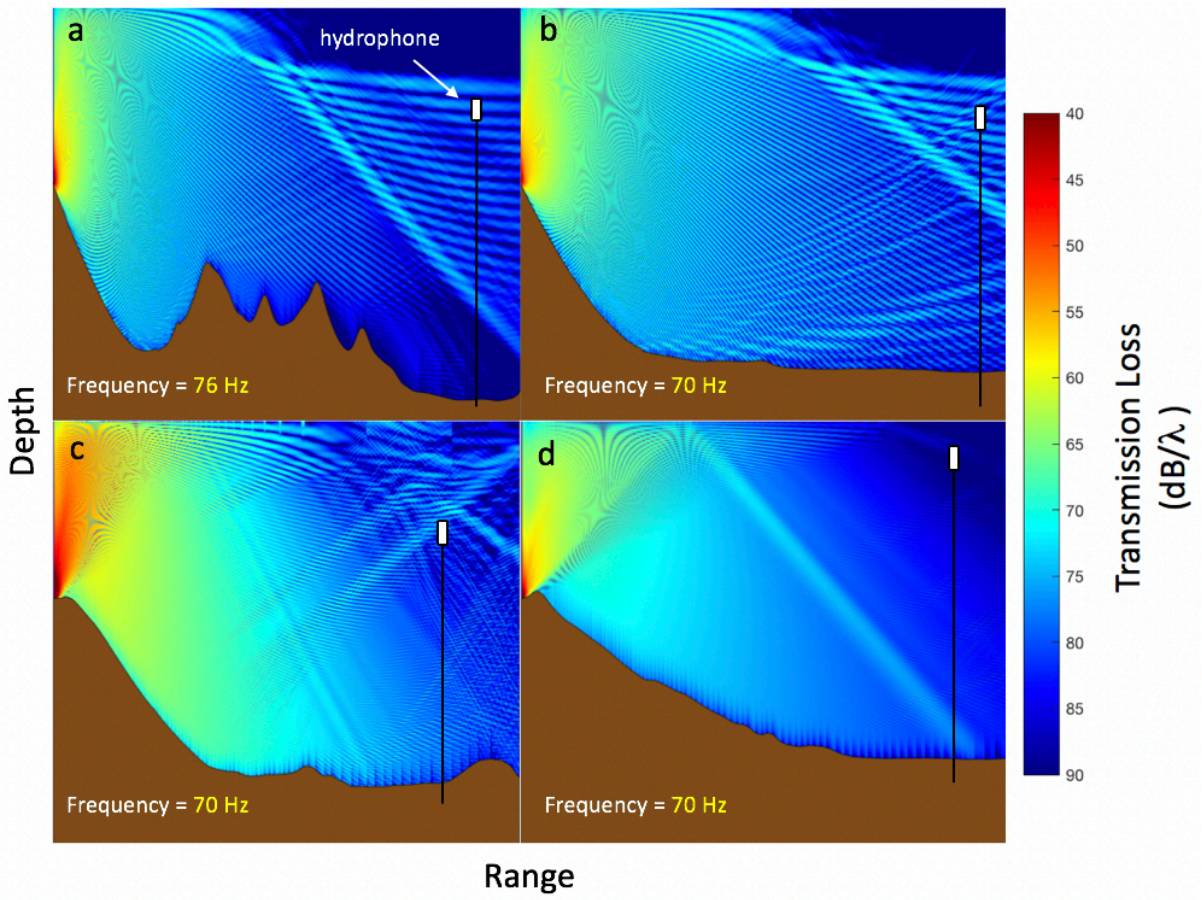

Fig. 19. Bellhop models generated for a source at 1480 m depth in the PIII region. a. north station; b. west station; c. east station; d. south station. Modeling shows a predictable pattern of transmission loss (TL) zones near the north and west stations. The east station shows a random arrangement of transmission loss zones and the south station lacks a pattern of TL zones. Bathymetric profiles are not to scale.

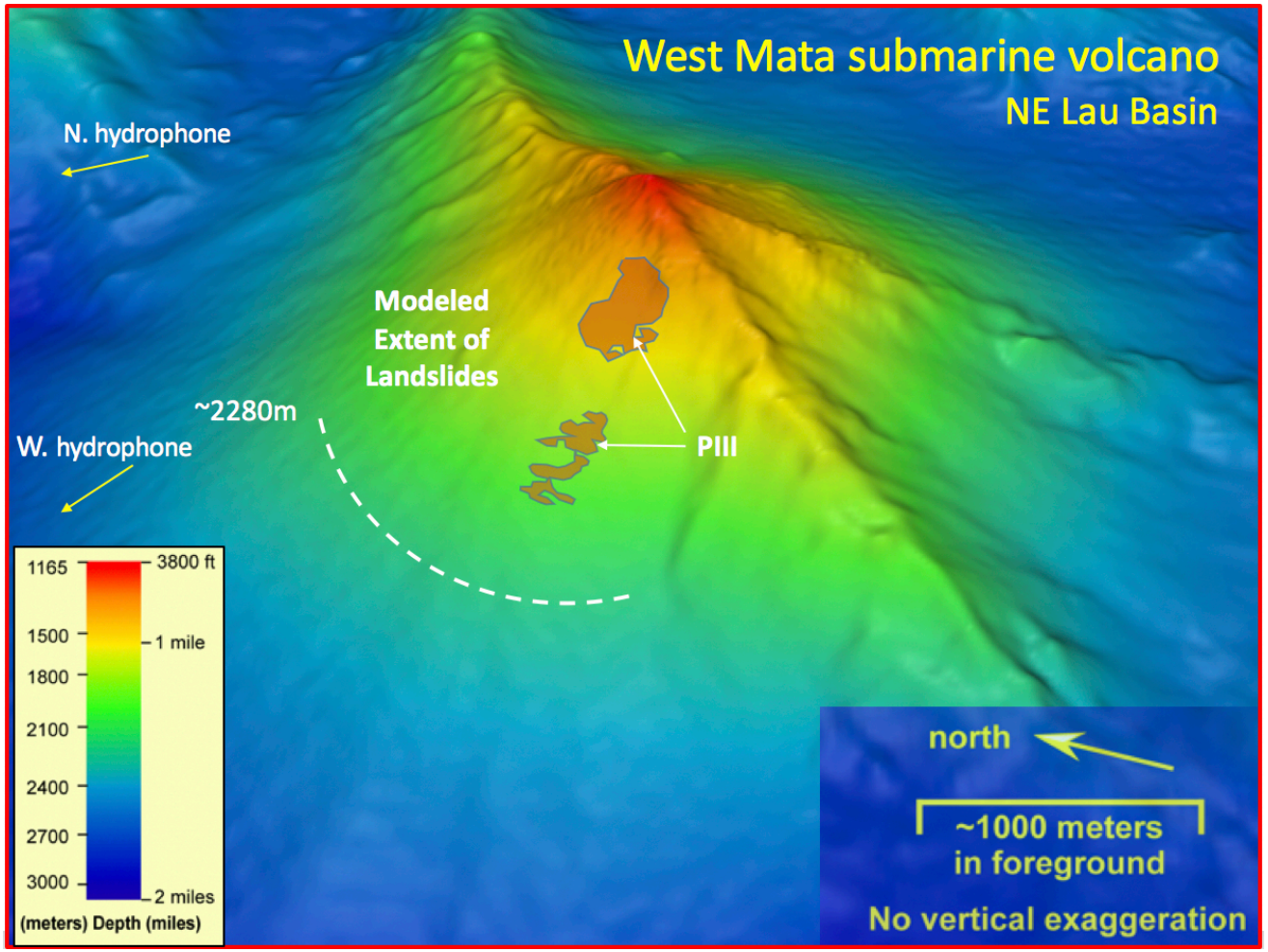

Fig. 20. 3D depiction of West Mata volcano showing the extent of modeled landslides on West Mata including the PIII eruptives region and downslope deposits mapped by Embley et al., 2015. Slides were found to occur on the western face between the summit and ~2280 m depth, consistent with the PIII eruptives region. These depths are based on 214 modeled landslides. Figure modified from NOAA ocean explorer website.

a. North station (figure caption continued on next page).

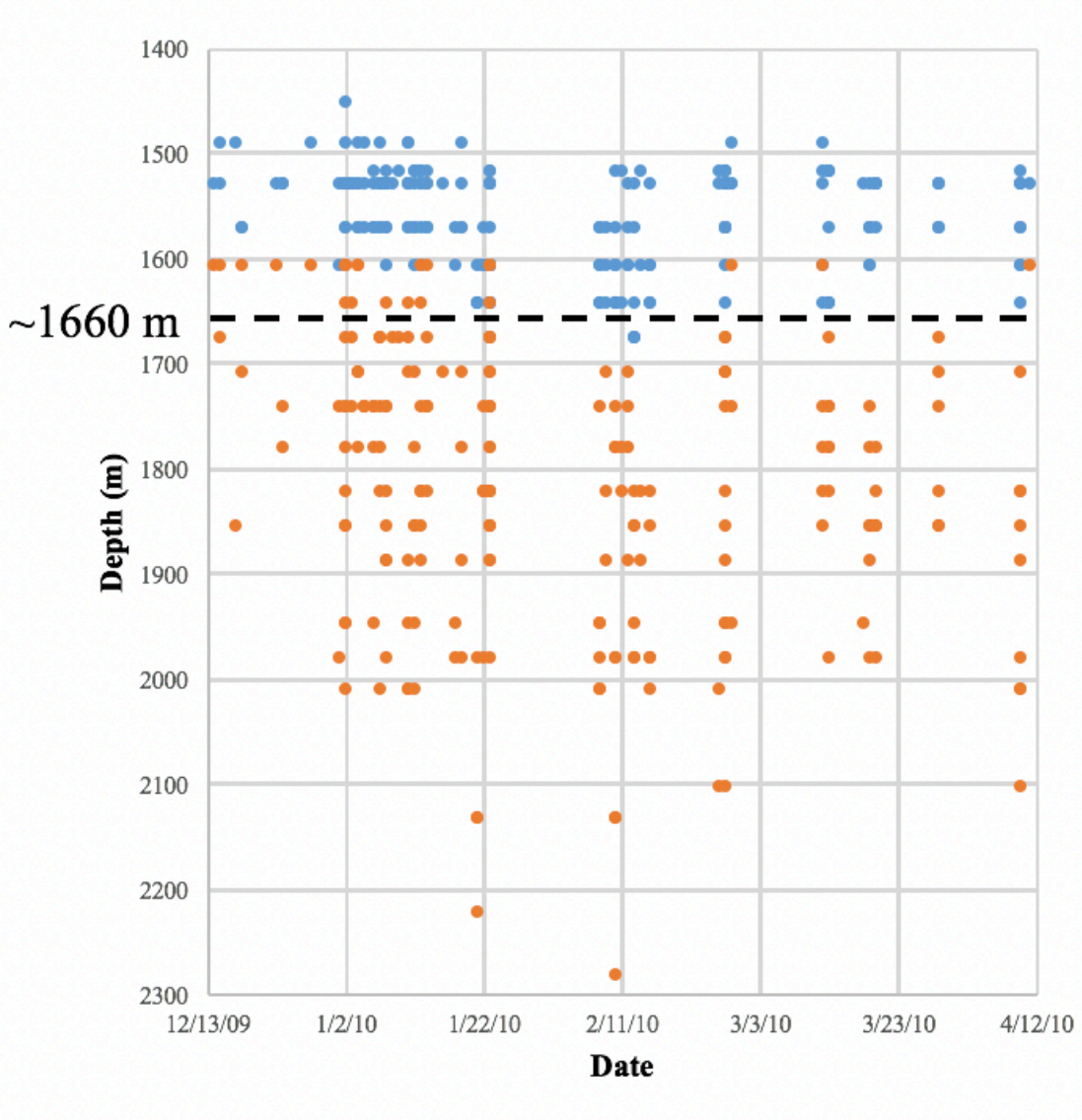

b. West station

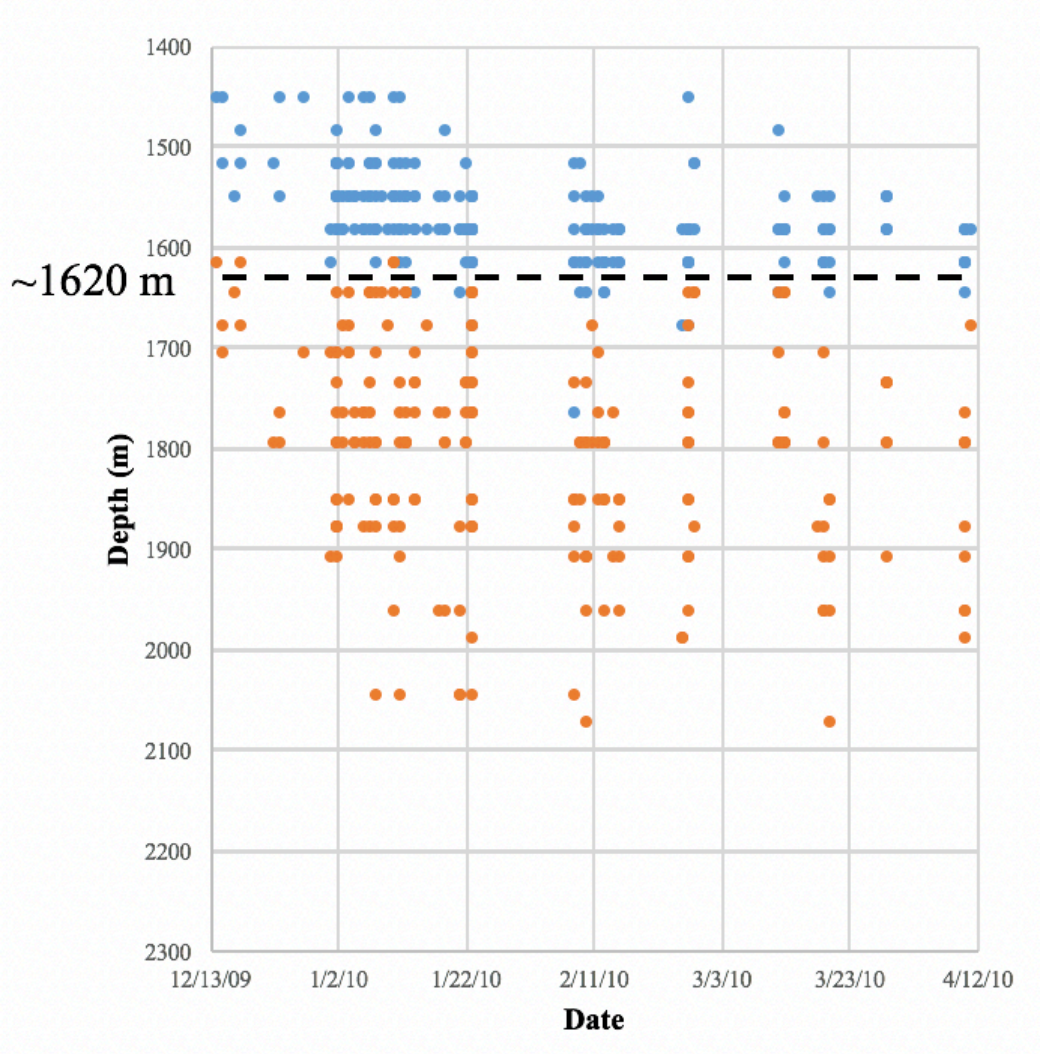

Fig. 21. Spread of landslide depths modeled by the north station (a) and west station (b). Slides initiated at depths marked in blue and ended at depths marked in orange. A greater range of end depths is observed in comparison to the start depths. The black dotted line represents a threshold that separates at least 90% of start depths from end depths. This threshold is slightly shallower based on western station models than northern station models.

a. North station

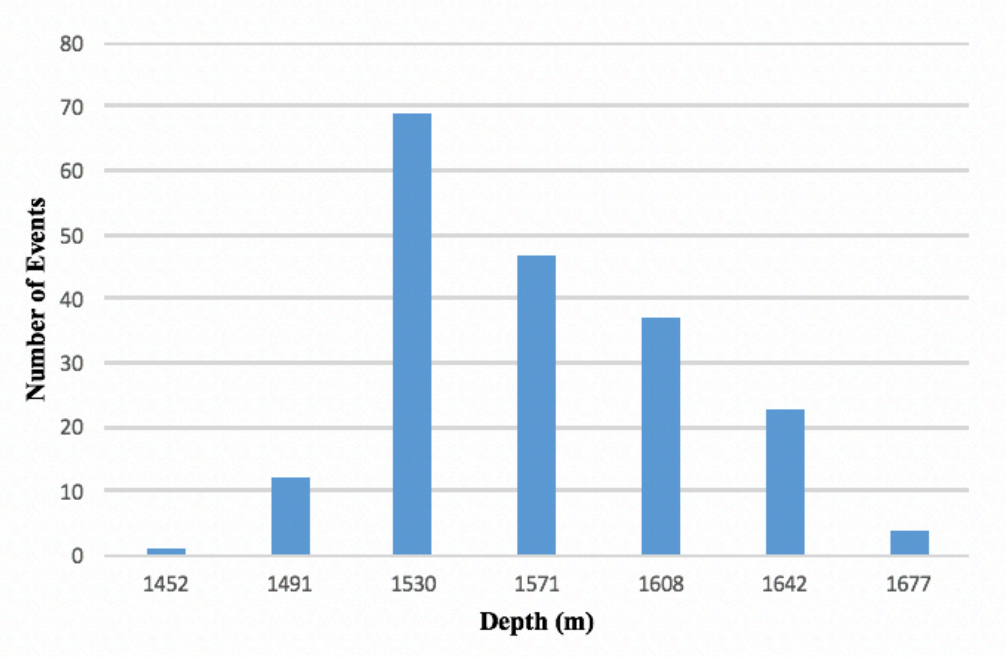

b. West station

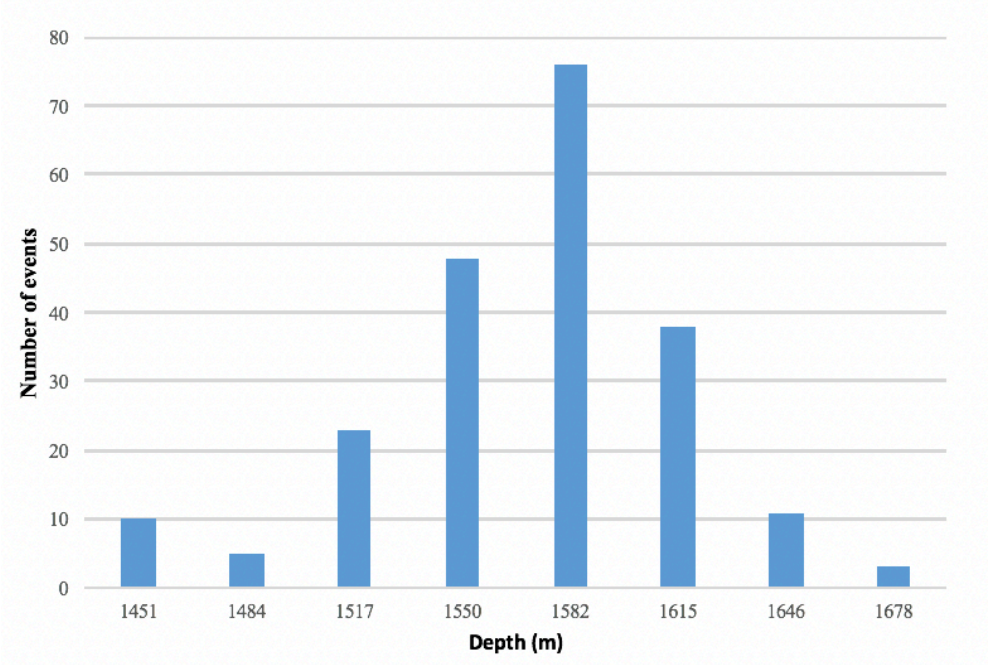

Fig. 22. Number of landslides per failure depth as modeled by the north station (a) and west station (b). North models show the most common failure depths occur between 1530 m and 1571 m. West models show the most common failure depths are between 1550 m and 1582 m. Bins were limited to the minimum data point spacing along bathymetric transects.

a. Initiation depths (figure caption continued on next page).

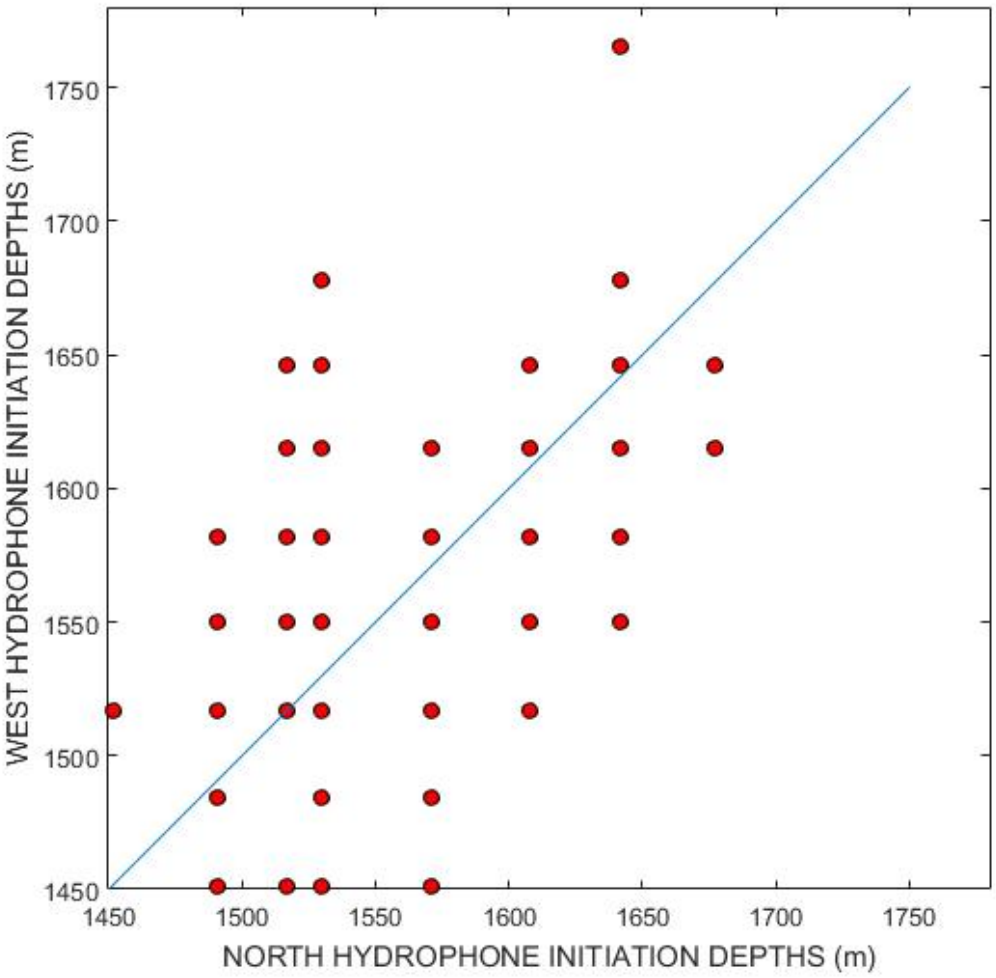

b. Termination depths

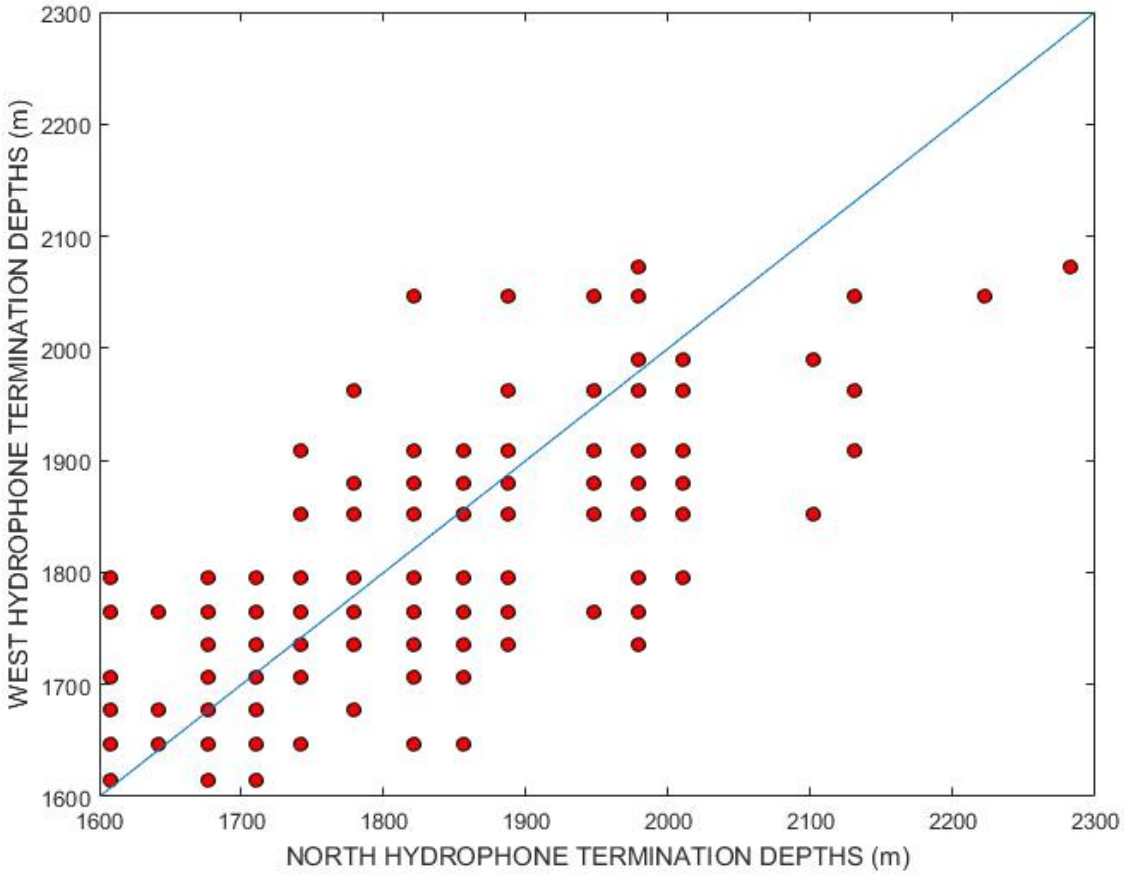

Fig. 23. Initiation depths and termination depths for landslides were compared between north and west models. Depths were modeled at best to +/- 20 m. Initiation depths appear to agree better than termination depths. The north models predict slightly deeper termination depths than the west models, which could be caused by the lack of local sound speed profile for modeling. Each data point may represent a few landslides with the same source depth, which is why there appears to be fewer samples for initiation depth.

a. North station

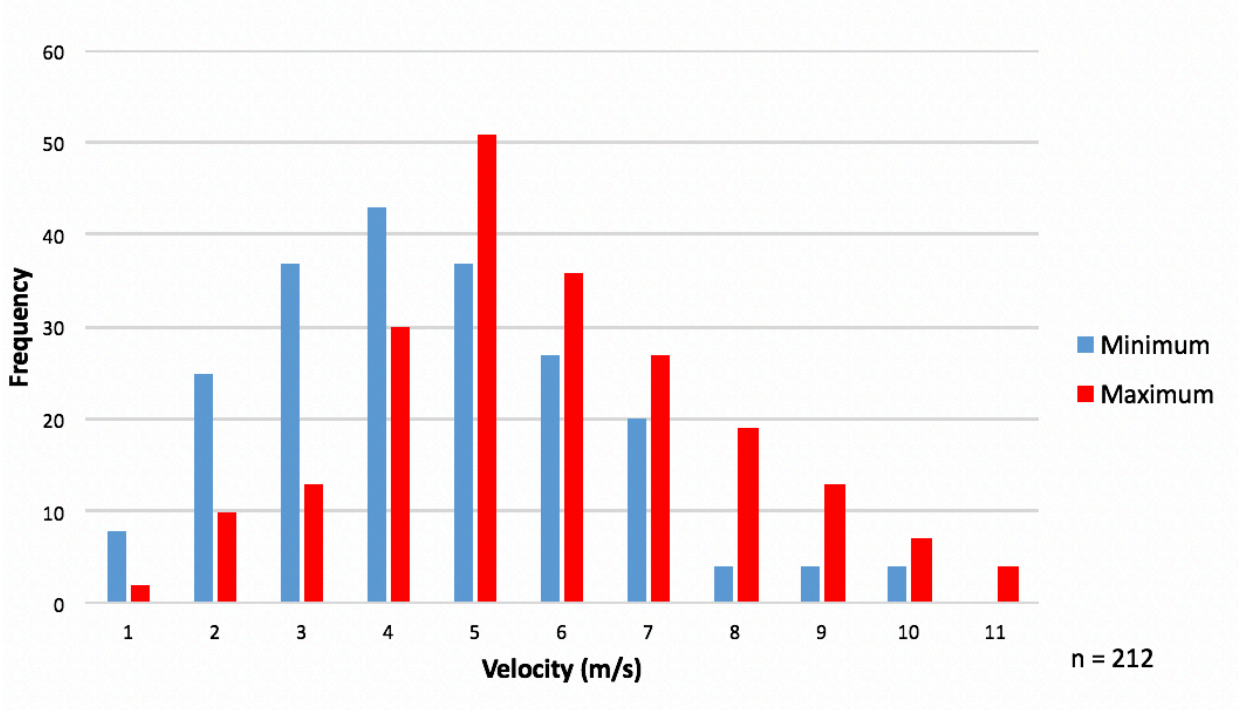

b. West station

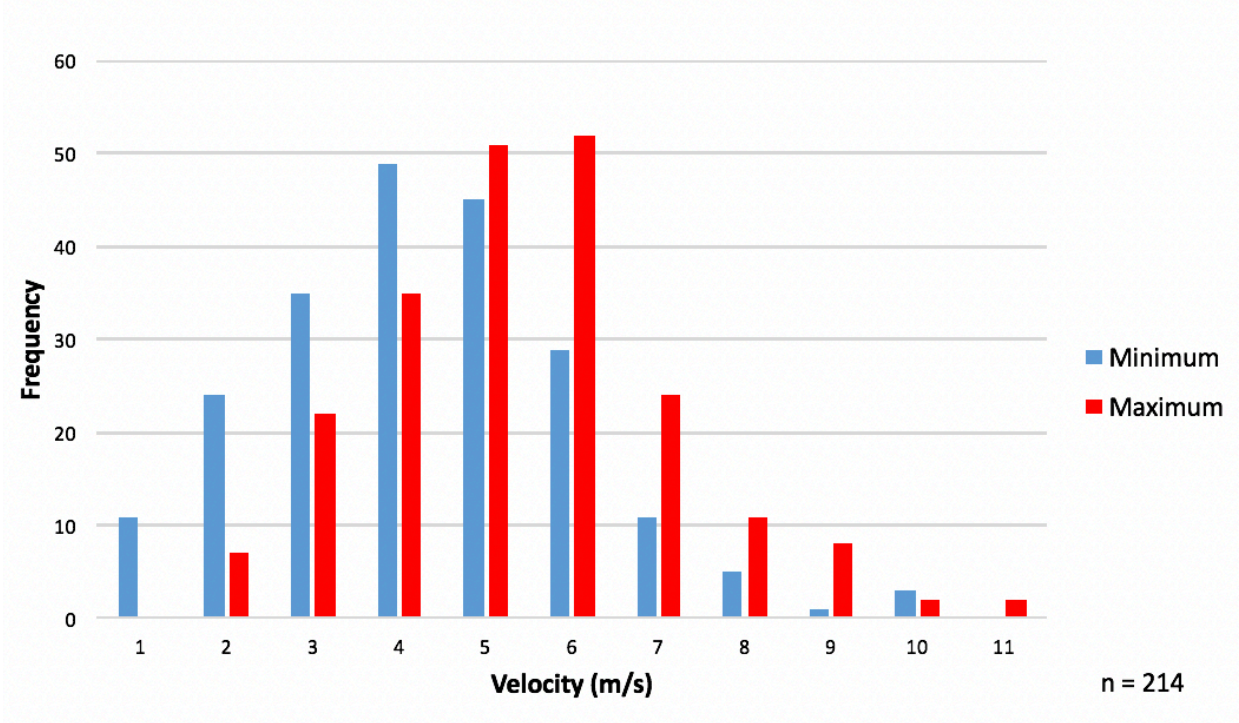

Fig. 24. Landslide velocities modeled from the north station (a) and the west station (b). Velocities typically hover between 4-6 m/s for both north and west models.

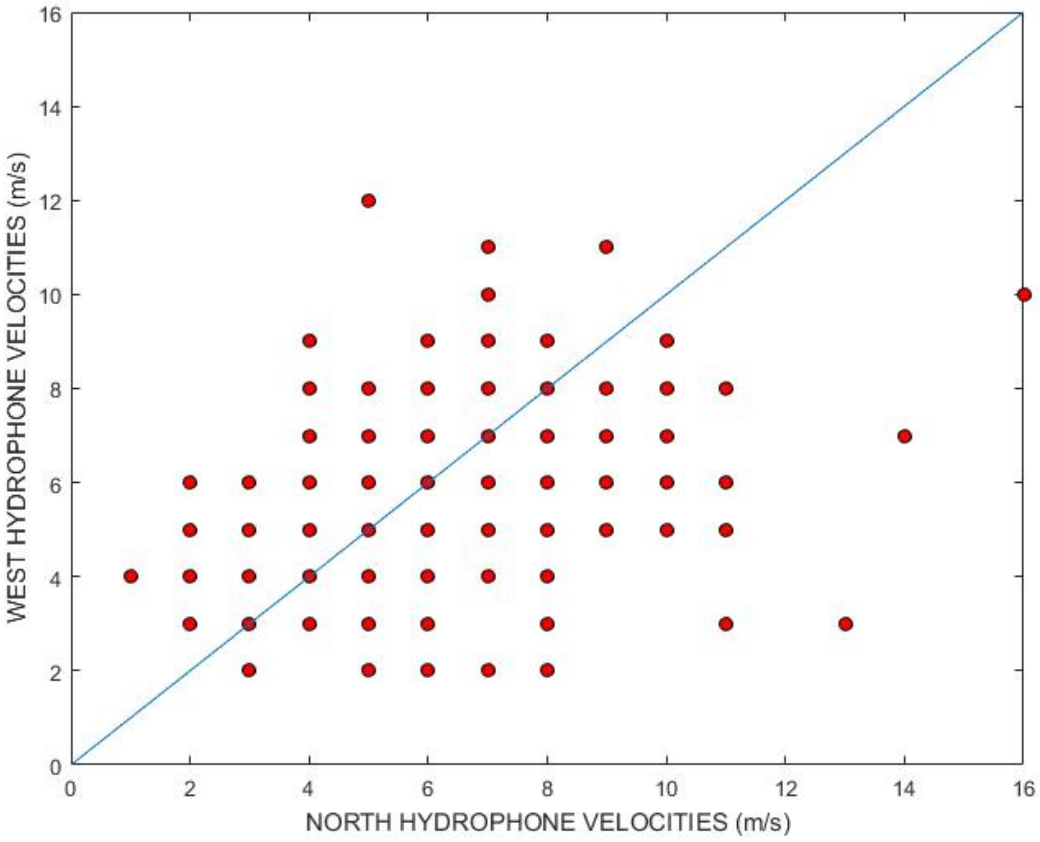

Fig. 25. Slide velocities compared between north and west models. Each data point may represent a number of slide velocities with the same value. Perfect agreement between models is represented by the blue line. Slide velocities differ between models by up to 7 m/s.

a. North station models.

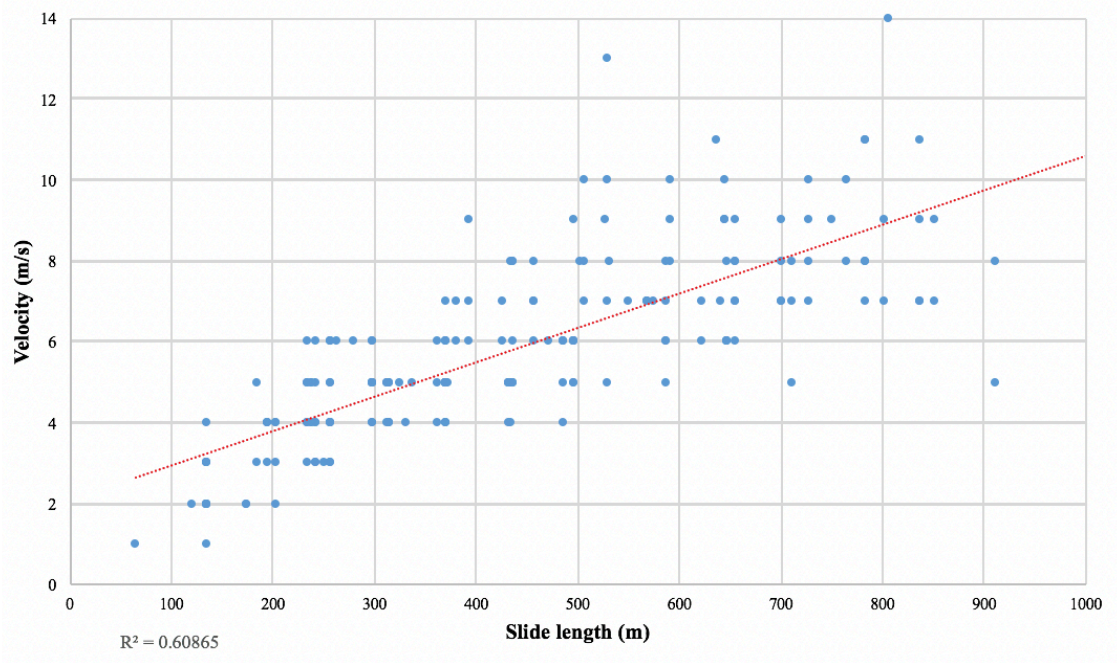

b. West station models.

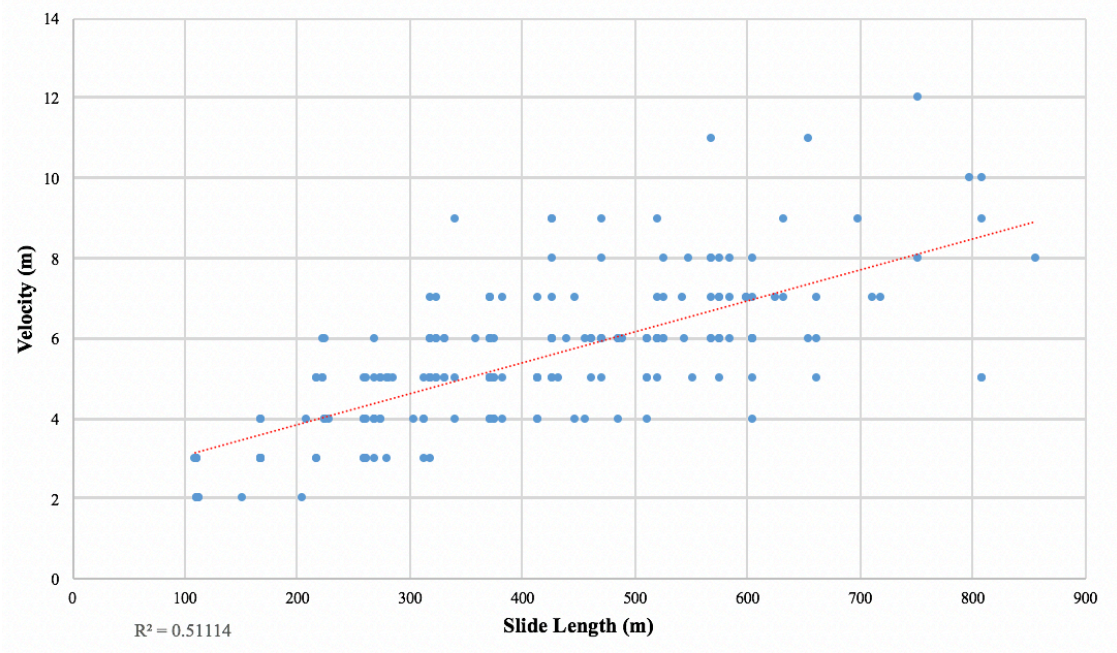

Fig. 26. Plots displaying landslide size (slide length) vs velocity. Large slides tend to travel fastest for both station models. Red lines represent best fit.

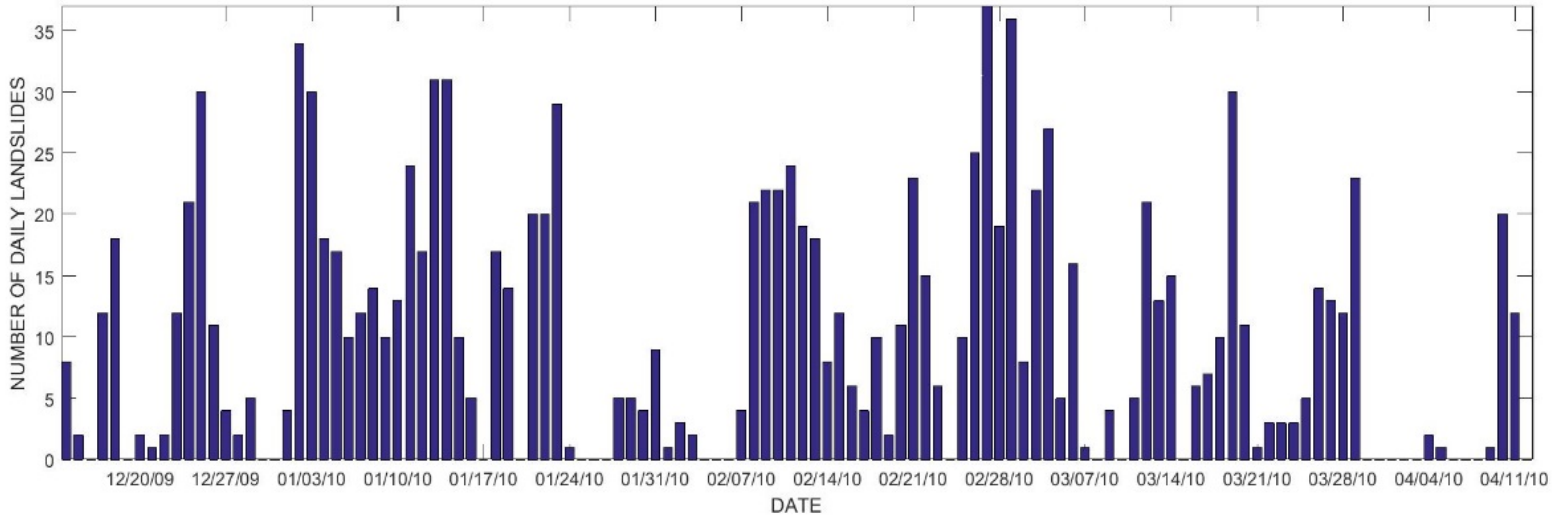

Fig. 27. Daily landslides occurring on West Mata (modified from (Caplan-Auerbach, Chadwick, et al., 2014)). Many days contain >30 separate events. Landslides during this 5-month period tend to cluster during active eruptive modes. These clusters were investigated further in an effort to interpret smaller scale landslide kinematics.

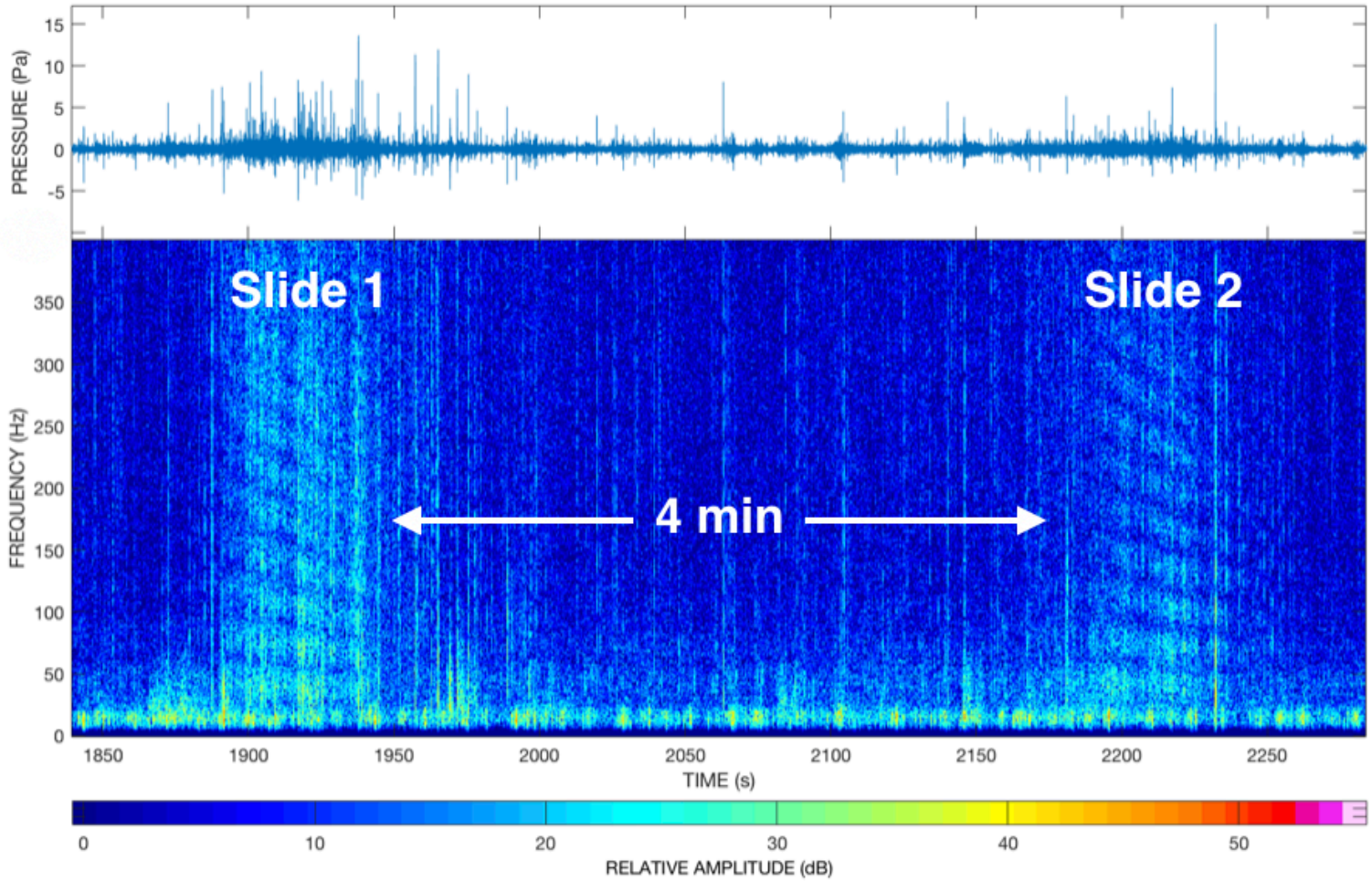

Fig. 28. Two landslides occurring ~4 minutes apart recorded by the north station. Each slide has roughly the same duration with similar interference patterns. Hydroacoustic similarity suggests that they occurred around the same location. It is not unusual for landslides to occur minutes apart during cluster events.

(a) January 2, 2010 (figure caption continued on next page).

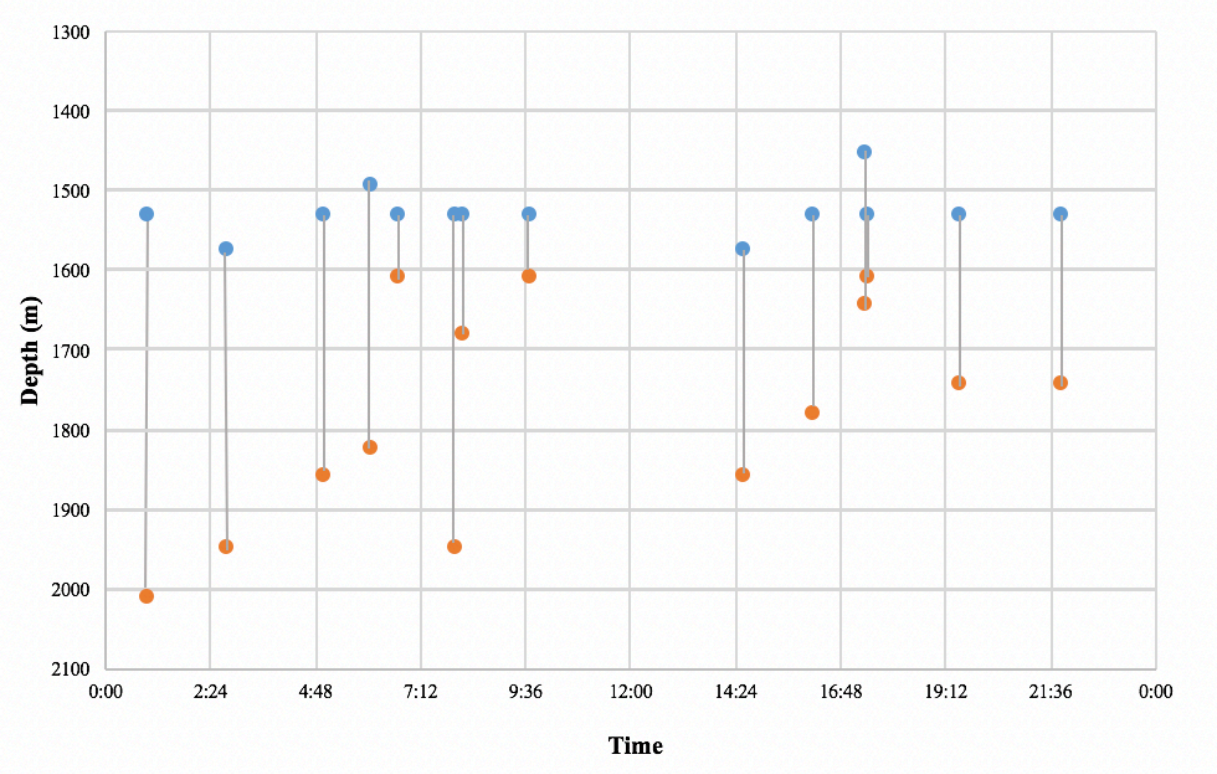

(b) January 23, 2010

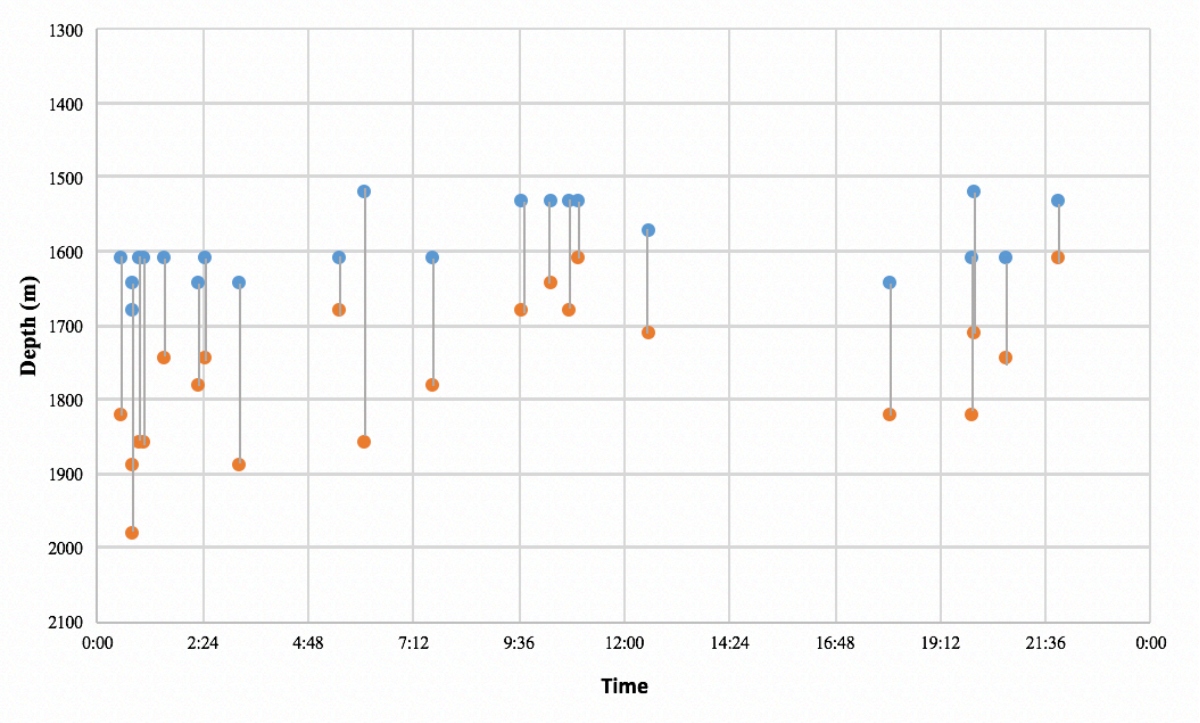

(c) February 26, 2010

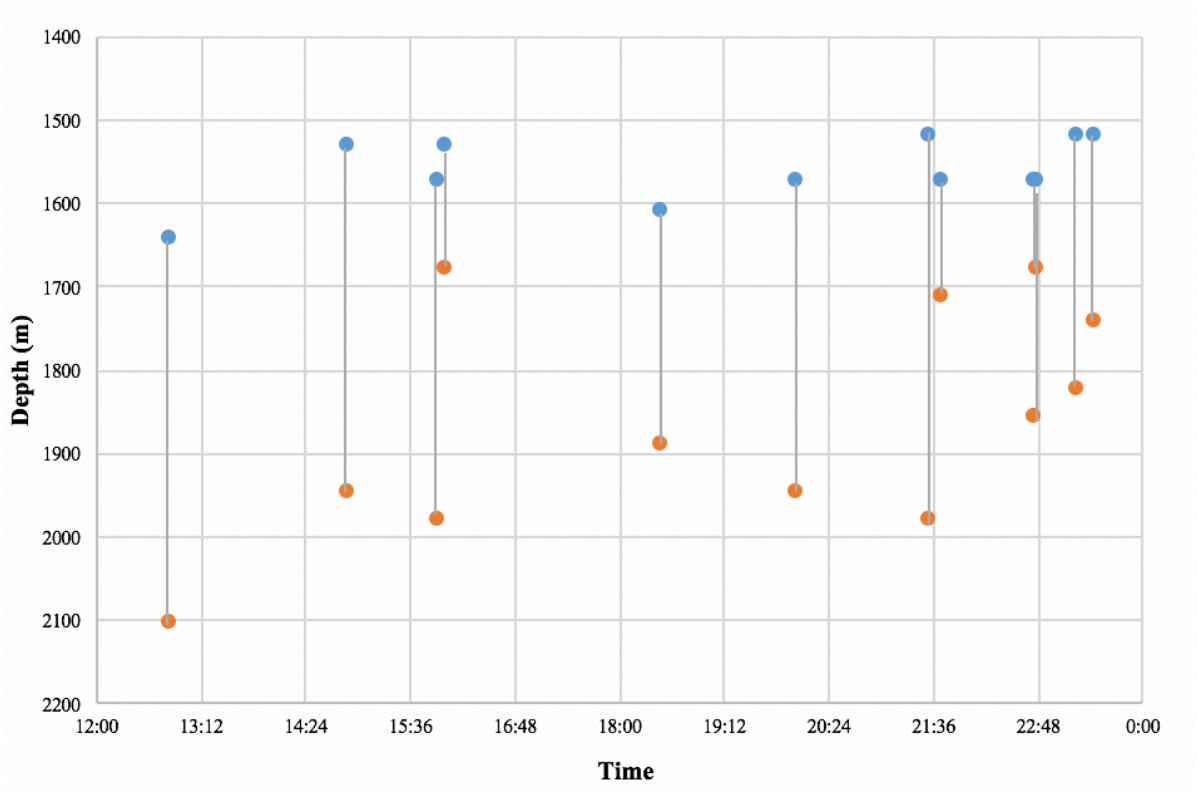

Fig. 29. Landslide run-outs during slide clusters modeled from the north station. (a) January 2, 2010. (b) January 23, 2010. (c) February 26, 2010. Blue dots are failure depths and orange dots are termination depths. Lines connecting points mark total run out distance for each slide. Slides tend to initiate at similar depths (~1550 m), but decrease in run out distance throughout the day. Even with +/- 20 m uncertainty in modeled depths, run out distances clearly decrease throughout the duration of these clusters.

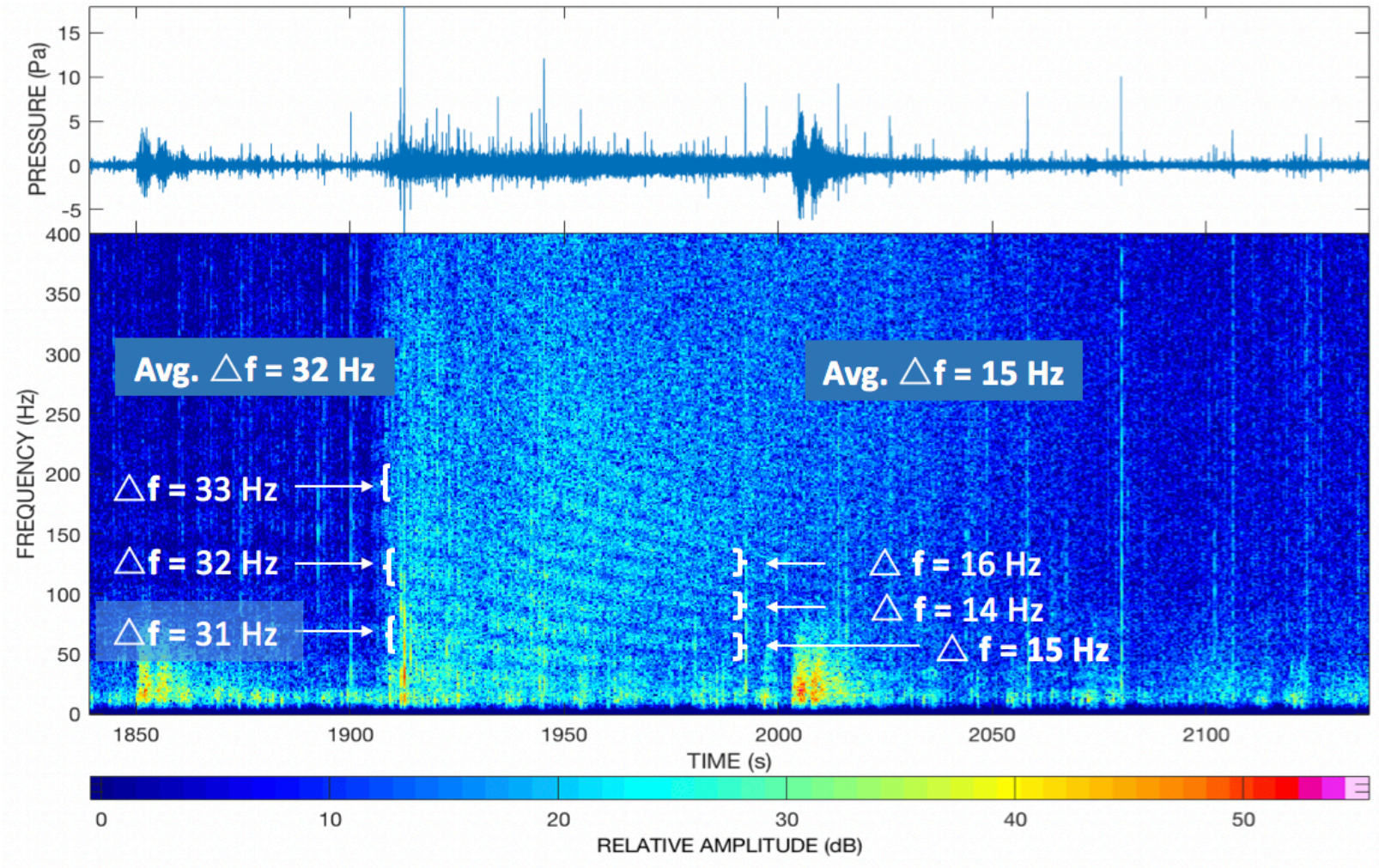

Fig. 30. Frequency spacing was calculated by taking an average of visible band spacing at the beginning of the signal and at the end of the signal. This method was used to calculate source depths for all landslide models. Low frequency pulses are not related to the landslide signal, but can sometimes affect its clarity.

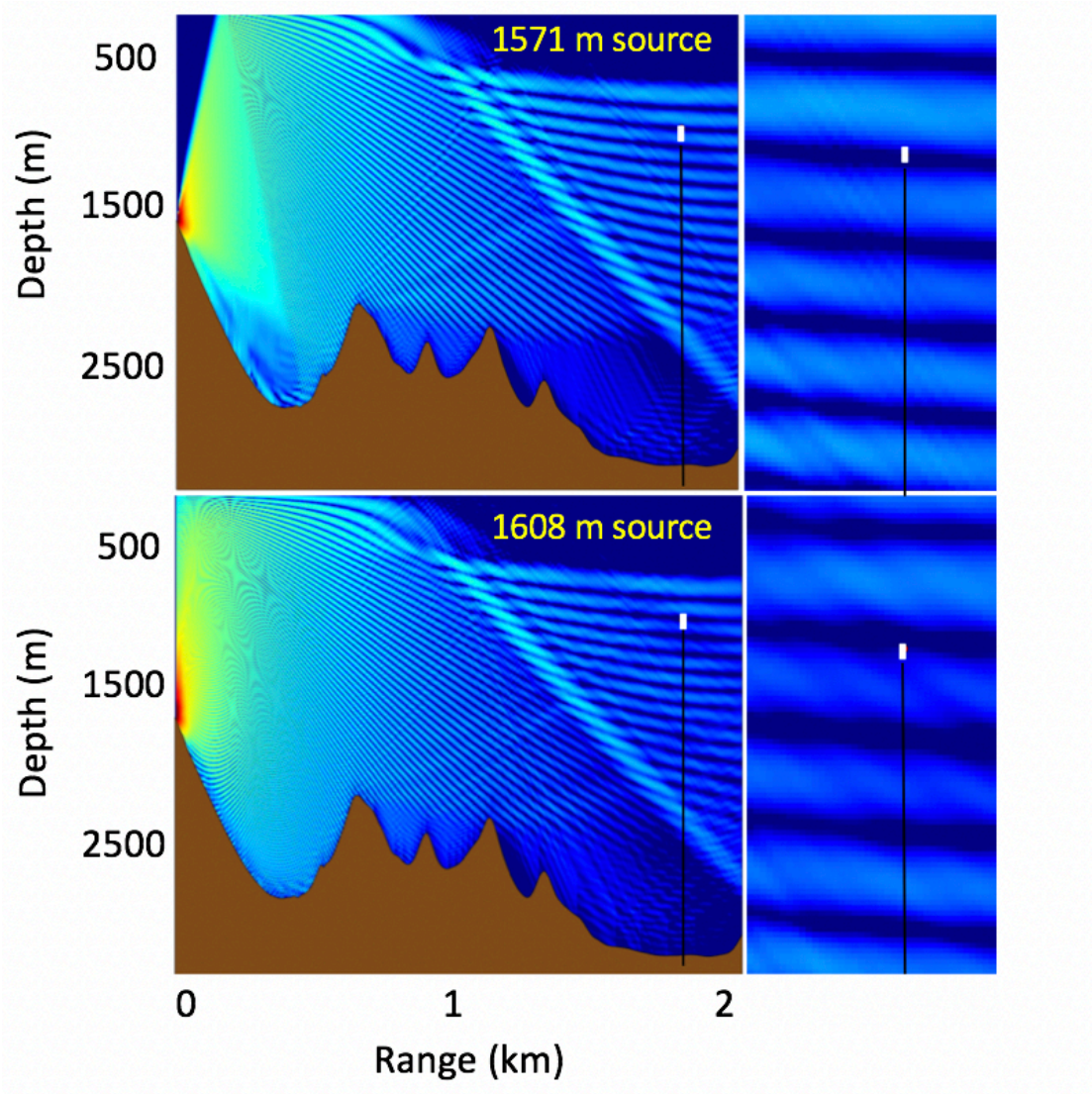

Fig. 31. Hypothetical acoustic sources (36 Hz) at 1571 m and 1608 m depth. Models show that there is a range of depths that would display the same interference pattern on the hydrophone. Acoustic sources occurring between 1571 m and 1608 m depth would place the hydrophone within the same zone of transmission loss, displaying the same spectral band pattern. On average, spectral bands change with every ~40 m depth change.

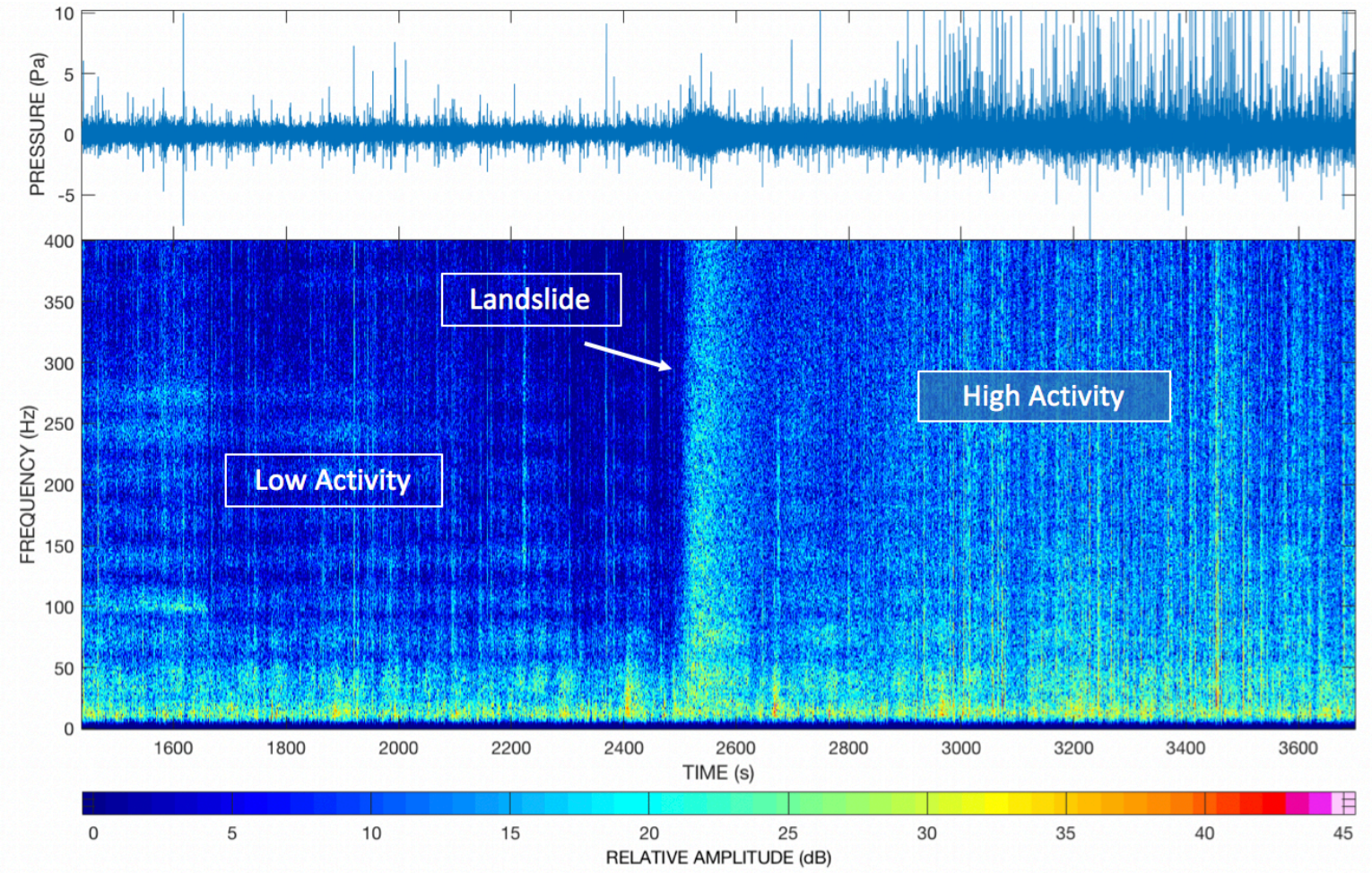

Fig. 32. A landslide signal here marks an increase in overall hydroacoustic background noise. Low background activity is dominated by frequencies <100 Hz whereas high background activity shows overall higher amplitude signal on a broadband scale. Landslides have been observed during periods of high activity and at times cause a change from low to high background activity.

Table 1: Hydrophone network (December 2009 - April 2010).

	North	**West**	**East**	**South**
Distance from West Mata summit (m)	18600	14000	10000	5630
Hydrophone depth (m)	912	955	897	230

Table 2. Real time arrivals for selected landslides. Arrivals for each station are delayed relative to the southern station due to varying distances from West Mata. Expected delays are based using a hydroacoustic velocity of 1482 m/s.

Station	**Slide 17**	**Slide 96**	**Slide 164**	**Avg. Delay (s)**	**Expected Delay (s)**
South	4:55:28	3:24:34	14:39:05	-	-
East	4:55:31	3:24:37	14:39:08	3.0	3.1
West	4:55:36	3:24:39	14:39:12	6.7	5.8
North	4:55:40	3:24:42	14:39:16	10.3	8.8

Table 3a. Statistical analysis for landslide velocities, north station.

	Slide Velocity (m/s)	
	Minimum	**Maximum**
Mode	4.0	5.0
Median	4.0	6.0
Mean	4.5	5.8
St. Dev.	2.0	2.1

Table 3b. Statistical analysis for landslide velocities, west station.

	Slide Velocity (m/s)	
	Minimum	**Maximum**
Mode	4.0	6.0
Median	4.0	5.0
Mean	4.3	5.5
St. Dev.	1.8	1.8

VIII. APPENDICES

APPENDIX 1 – MATLAB SCRIPTS

- hydrophone_mata.m – *reads in .DAT files from the hydrophone network to be analyzed on a hydroacoustic spectrogram. Courtesy of Jacqueline Caplan-Auerbach.*

- hydrophone_corr.m – *Converts raw hydrophone data from counts to Pascals. Courtesy of Del Bohnenstiehl.*

- jspecgram2.m – *generates a hydroacoustic spectrogram from .DAT files recorded by the hydrophone network. Courtesy of Jacqueline Caplan-Auerbach.*

- jfiltfilt.m – *filters the signal (high, low, bandpass), courtesy of Jacqueline Caplan-Auerbach..*

- slidetime.m –*calculates arrival time and duration of landslide signals.*

- avg_interference.m – *calculates average spacing of interference bands on a number of selections.*

- bty_shift.m – *converts bathymetric .txt file to a form readable by Bellhop hydroacoustic modeling program. Bathymetric profiles were extracted from GeoMapApp.*

APPENDIX II – BELLHOP HYDROACOUSTIC MODEL

- Bellhop is a program that models hydroacoustic wave propagation by beam scattering and transmission loss (Porter, 2011). Transmission loss models were generated using environmental files that contained information regarding the sound field environment. Bellhop was called in Matlab using the command <<bellhop '.envfilename', which then called the environmental and bathymetry files to calculate transmission loss, illustrated by a sound field image.

APPENDIX III – OTHER

a. The landslide catalog containing source depths and velocities calculated by interference spacing is on an Excel file available by request.

b. An Excel catalog of source depths modeled by interference pattern is available by request.

c. Hydrophone coordinates are available by request.